Combined Effect of Organic Carbon and Arsenic on the Formation of Sediment-Hosted Gold Deposits: A Case Study of the Shahuindo Epithermal Deposit, Peru

Jean Vallance, Renzo Galdos, Macneill Balboa, Brigitte Berna, Omar Cabrera, Freddy Huisa, Camille Baya, Caroline van de Vyver, Willem Viveen, Didier Béziat, et al.

Economic Geology, v. 119, no. 1, pp. 85–112

Combined Effect of Organic Carbon and Arsenic on the Formation of Sediment-Hosted Gold Deposits: A Case Study of the Shahuindo Epithermal Deposit, Peru

Jean Vallance,[1,2,†] Renzo Galdos,[1] Macneill Balboa,[1] Brigitte Berna,[1] Omar Cabrera,[3] Freddy Huisa,[3] Camille Baya,[4] Caroline Van De Vyver,[4] Willem Viveen,[5] Didier Béziat,[4] Stefano Salvi,[4] Stéphane Brusset,[4] Patrice Baby,[4,5] and Gleb S. Pokrovski[4]

[1]*Grupo de investigación en Geología de Yacimientos, Especialidad de Ingeniería Geológica, Departamento de Ingeniería, Pontificia Universidad Católica del Perú, avenida Universitaria 1801, San Miguel, Lima 15088, Peru*

[2]*Thin Section Lab, 1223 Rue du Bois la ville, F-54200 Toul, France*

[3]*Pan American Silver Peru S.A.C., Av. de la Floresta 497, Lima 15037, Peru*

[4]*Géosciences Environnement Toulouse, Université Toulouse III - Paul Sabatier, Centre National de la Recheche Scientifique (CNRS), Institut de Recherche pour le Développement (IRD), Centre National d'Etudes Spatiales (CNES), Observatoire Midi Pyrénées (OMP), 14 avenue Edouard Belin, F-31400 Toulouse, France*

[5]*Grupo de investigación en Geología Sedimentaria, Especialidad de Ingeniería Geológica, Departamento de Ingeniería, Pontificia Universidad Católica del Perú, avenida Universitaria 1801, San Miguel, Lima 15088, Peru*

Abstract

Sediment-hosted gold deposits represent a significant portion of the world's gold resources. They are characterized by the ubiquitous presence of organic carbon (C_{org}; or its metamorphosed product, graphite) and the systematic occurrence of invisible gold-bearing arsenian pyrite. Yet the role played by these features on ore formation and the distribution of gold remains a long-standing debate. Here, we attempt to clarify this question via an integrated structural, mineralogical, geochemical, and modeling study of the Shahuindo deposit in northern Peru, representative of an epithermal gold deposit contained in a sedimentary basin. The Shahuindo deposit is hosted within Lower Cretaceous fluvio-deltaic carbon-bearing sandstone, siltstone, and black shale of the Marañón fold-and-thrust belt, where intrusions of Miocene age are also exposed. The emplacement of the auriferous orebodies is constrained by structural (thrust faults, transverse faults) as well as lithological (intrusion contacts, permeable layers, anticlinal hinge in sandstone) features. The defined gold reserves (59 tons; t) are located in the supergene zone in the form of native gold grains. However, a primary mineralization, underneath the oxidized zone, occurs in the form of invisible gold in arsenian pyrite and arsenopyrite. Here, four subsequent pyrite generations were identified—namely, pyI, pyII, pyIII, and pyIV. PyI has mean Au concentrations of 0.3 ppm, contains arsenic that is not detectable, and is enriched in V, Co, Ni, Zn, Ag, and Pb compared to the other pyrite generations. This trace element distribution suggests a diagenetic origin in an anoxic to euxinic sedimentary basin for pyI. Pyrite II and pyIV have comparable mean Au (1.1 and 0.7 ppm, respectively) and As (2.4 and 2.9 wt %, respectively) concentrations and precipitated under conditions evolving from lower (pyrrhotite, chalcopyrite, sphalerite) to higher (enargite, digenite, chalcocite) sulfidation, respectively. The pyIII generation is the major gold event in the primary mineralization, with pyrite reaching 110 ppm Au (mean ~7 ppm) and 5.6 wt % As (mean ~1.8 wt %), while coeval arsenopyrite attains 460 ppm Au. Pyrite III is also enriched in other trace elements such as Se, Ge, Mo, In, Ga, and Bi compared to the other pyrite generations, which is indicative of a magmatic source. Bulk analyses of the surrounding unmineralized rocks show only parts per billion levels of Au and less than 25 ppm As. These data, combined with mass balance considerations, demonstrate that the sedimentary rocks could not be the sole source of gold, as they could only contribute a minor portion of arsenic and sulfur (and iron) to the deposit. Conversely, fluids exsolved from a pluton crystallizing at depth likely provided the great part of the gold endowment. Equilibrium thermodynamics simulations, using geochemical constraints established in this study, demonstrate that interaction between Au-As-S-Fe–bearing fluids and organic carbon-bearing rocks strongly enhanced the fluid ability to transport gold by maximizing its solubility as Au^{I} hydrosulfide complexes via a combined increase of pH and aqueous sulfide concentration. This finding challenges the traditional qualitative view of organic matter acting exclusively as a reducing agent for Au^{I} that should promote gold deposition in its native state (Au^{0}) rather than enhance its solubility in the fluid. Our results have significant implications for the exploration of carbonaceous sedimentary environments. Such settings may provide a very effective mechanism for focusing gold transport. Subsequent scavenging of Au^{I} from solution in a chemically bound form is promoted by the precipitation of arsenian pyrite in permeable structural and lithologic traps, bound by more impermeable units, similar to what occurs in petroleum systems. Our integrated study underlines the important potential of sedimentary C_{org}-bearing rocks in the formation and distribution of gold and associated metal resources.

[†]Corresponding author: e-mail, jeanvallance@hotmail.com

ISSN 0361-0128; doi:10.5382/econgeo.5040; 28 p.
Digital appendices are available in the online Supplements section.

Submitted: August 25, 2022 / Accepted: April 29, 2023

Introduction

Sediment-hosted deposits represent an important part of gold resources on Earth. Examples of mineralization in siliciclastic sedimentary rocks that contain gold as the main product or by-product can be found in at least six (orogenic, porphyry, epithermal, Carlin-type, reduced intrusion-related, and volcanogenic massive sulfide) out of the 11 gold deposit classes proposed by Sillitoe (2020). Notwithstanding the classification and exact source of gold (e.g., magmatic, metamorphic, sedimentary, or biogenic), the most characteristic features of sediment-hosted gold deposits are the systematic presence of organic carbon (C_{org}, i.e., bitumen, pyrobitumen, or their metamorphosed product, graphite) and arsenian pyrite (e.g., Cline et al., 2005; Large et al., 2009; Muntean et al., 2011; Gaboury, 2013; Gregory et al., 2016; Percival et al., 2018; Xie et al., 2018). The respective roles of these ubiquitous features as a possible gold source and their impact on the processes of metal concentration and/or remobilization are long-standing subjects of debate. Some authors consider the carbonaceous sediments to be both the source and trap for mineralization, which was produced by hydrothermal processes at local to regional scale within the crust (e.g., Phillips et al., 1987; Large et al., 2011; Hofstra and Cline, 2000). Other studies defend a magmatic source and vapor-phase transport of gold, with carbonaceous sediments acting exclusively as a metal trap (e.g., Muntean et al., 2011; Large et al., 2016; Muntean and Cline, 2018).

There exist multiple instances of close spatial and temporal associations of gold with organic matter, such as in the renowned Witwatersrand basin, where the precipitation of native gold and uraninite was suggested to have occurred by reduction at the interface between a hydrothermal sulfide-bearing fluid and hydrocarbon liquids or solids (Disnar and Sureau, 1990; Robb and Meyer, 1995; Drennan et al., 1999; Drennan and Robb, 2006; Fuchs et al., 2016). The close spatial association of gold and carbonaceous-bearing formations (including hydrocarbons) in the Carlin trend deposits has triggered the foundation for the carbonaceous trap model (Radtke and Scheiner, 1970). However, more recent work on Carlin deposits has shown that organic carbon contents and ore grades do not correlate, thus suggesting that C_{org} likely played only a minor role (if any) in gold concentration and precipitation, compared to the major gold precipitation mechanism through sulfidation of ferroan carbonates (Hofstra and Cline, 2000; Cline et al., 2005; Kusebauch et al., 2019; Muntean, 2020). Gold transport and concentration are known to result from a complex interplay of different parameters (temperature [T], pressure [P], pH, redox, S content) of the fluid during its evolution and interactions with the host rock (e.g., Seward, 1973; Heinrich, 2005; Pokrovski et al., 2014). However, quantification of the respective contributions of these parameters is lacking for sedimentary deposit settings. It also remains unclear whether gold may be transported to a significant degree by the liquid hydrocarbon phases as opposed to the aqueous phase. Rare experimental data on a wide range of crude oil samples at temperatures of 150° to 300°C show that gold solubilities are too low (e.g., <50 ppb; Migdisov et al., 2017) to allow for massive gold transport. Indeed, these low values contrast with thermodynamic predictions, multiple experimental studies, and extensive data from natural fluid inclusions, all of which demonstrate that an aqueous S-rich epithermal fluid (>0.1 wt % S), at equivalent temperatures, is capable of dissolving tens to hundreds of parts per million of Au, at favorable pH and redox conditions (e.g., Seward, 1973; Heinrich, 2005; Kouzmanov and Pokrovski, 2012; Pokrovski et al., 2014, 2022a; references therein). Thus, our current view on the mechanisms of formation of sedimentary gold deposits lacks a quantitative physicochemical understanding of the interactions that take place between a fluid and the rocks it flows through. This understanding is now possible by coupling the robust up-to-date knowledge of the chemical speciation and solubility of Au in aqueous fluids with a well-constrained geologic framework based on detailed studies of the ores and their host rocks.

Another serious limitation in understanding the transport and deposition of gold in sedimentary deposits is the role of arsenic, since arsenian pyrite and arsenopyrite are systematically enriched in invisible gold in these settings (e.g., Cathelineau et al., 1989; Reich et al., 2005; Deditius et al., 2014). Even though the redox and chemical state of gold and its incorporation mechanisms in these sulfides remain subjects of debate (e.g., Arehart et al., 1993; Pokrovski et al., 2019; references therein), recent experimental data attest to an enhanced Au partitioning from a hydrothermal fluid to As-bearing pyrite with increasing As content in the system (e.g., Kusebauch et al., 2019; Pokrovski et al., 2019, 2021). This partitioning data, together with the recent spectroscopic knowledge of the structural and redox state of invisible Au in sulfarsenides (e.g., Pokrovski et al., 2021; references therein) as well as improved thermodynamic and structural models of the incorporation of As into pyrite (e.g., Xing et al., 2019; Manceau et al., 2020), allow at present more quantitative modeling of the arsenic-gold relationships during fluid-rock interaction.

In this study, we attempt to unravel fundamental questions of the roles played by arsenic and organic carbon in the formation of sediment-hosted gold deposits. Here, we explore the Au-As-C_{org} relationships using, as a case study, the Shahuindo gold deposit in northern Peru, characterized by the presence of invisible gold associated with arsenian pyrite and organic matter in a sedimentary basin (Defilippi et al., 2016; Vallance et al., 2018). To interpret these features, we have combined detailed structural investigations of the formation and evolution of this sedimentary sequence with in situ microanalyses of ore and gangue minerals, followed by physicochemical modeling of fluid-mineral-organic carbon interactions. Our results provide new constraints on the controls exerted both by arsenic and C_{org} on gold transport and deposition. Our findings may be applicable to many other sediment-hosted deposits and thus contribute to improving exploration strategies for this important resource of gold and associated metals.

Geologic Background and Samples

Regional geology

The thousand-kilometer-long NNW-SSE–trending Marañón fold-and-thrust belt of central to northern Peru hosts a variety of ore deposits, including Cu-Mo-Au porphyry (e.g., Toromocho), polymetallic and Cu-Fe skarn (e.g., Antamina), and epithermal precious and base metals deposits (e.g.,

Yanacocha and Cerro de Pasco), genetically linked to Oligocene to Miocene subduction-related calc-alkaline magmatism (Noble and McKee, 1999; Bissig et al., 2008; Scherrenberg et al., 2016; Fontboté, 2018). This belt hosts, respectively, 40, 30, 75, and 65% of the Au, Cu, Zn, and Ag production of the country (Noble and McKee, 1999; Scherrenberg et al., 2016; Fontboté, 2018). In the study area, the rocks building the Marañón belt correspond to fluvio-deltaic and marine sediments of Late Jurassic to Late Cretaceous age, deposited in a back-arc basin on a basement of Precambrian to Lower Ordovician metamorphic rocks known as the Marañón Complex (Mégard, 1984; Benavides-Cáceres, 1999; Chew et al., 2007; Eude et al., 2015; Scherrenberg et al., 2016). The Marañón belt is truncated by a middle Eocene regional unconformity capped by volcanic and volcaniclastic sediments of the late Eocene to Middle Miocene Calipuy plateau basin to the west (Noble et al., 1990; Prudhomme et al., 2019) and the Cajabamba basin fluvial and lacustrine sediments to the east (Figs. 1, 2). The base of the Cajabamba deposits has recently been dated at ~23 Ma (Prudhomme et al., 2019). Therefore, the belt is considered to have developed during an early period of the Andean orogeny (traditionally known as Peruvian and Incaic phases; Noble et al., 1979; Mégard, 1984), between the Late Cretaceous and the middle Eocene. The Marañón belt is a thin-skinned thrust system related to a detachment located at the base of the Late Jurassic black shale and sandstone rocks of the Chicama Formation and composed by a succession of tight imbricates and associated folds, reflecting a significant amount of horizontal shortening. The post-Incaic orogenic period is characterized by the development of the

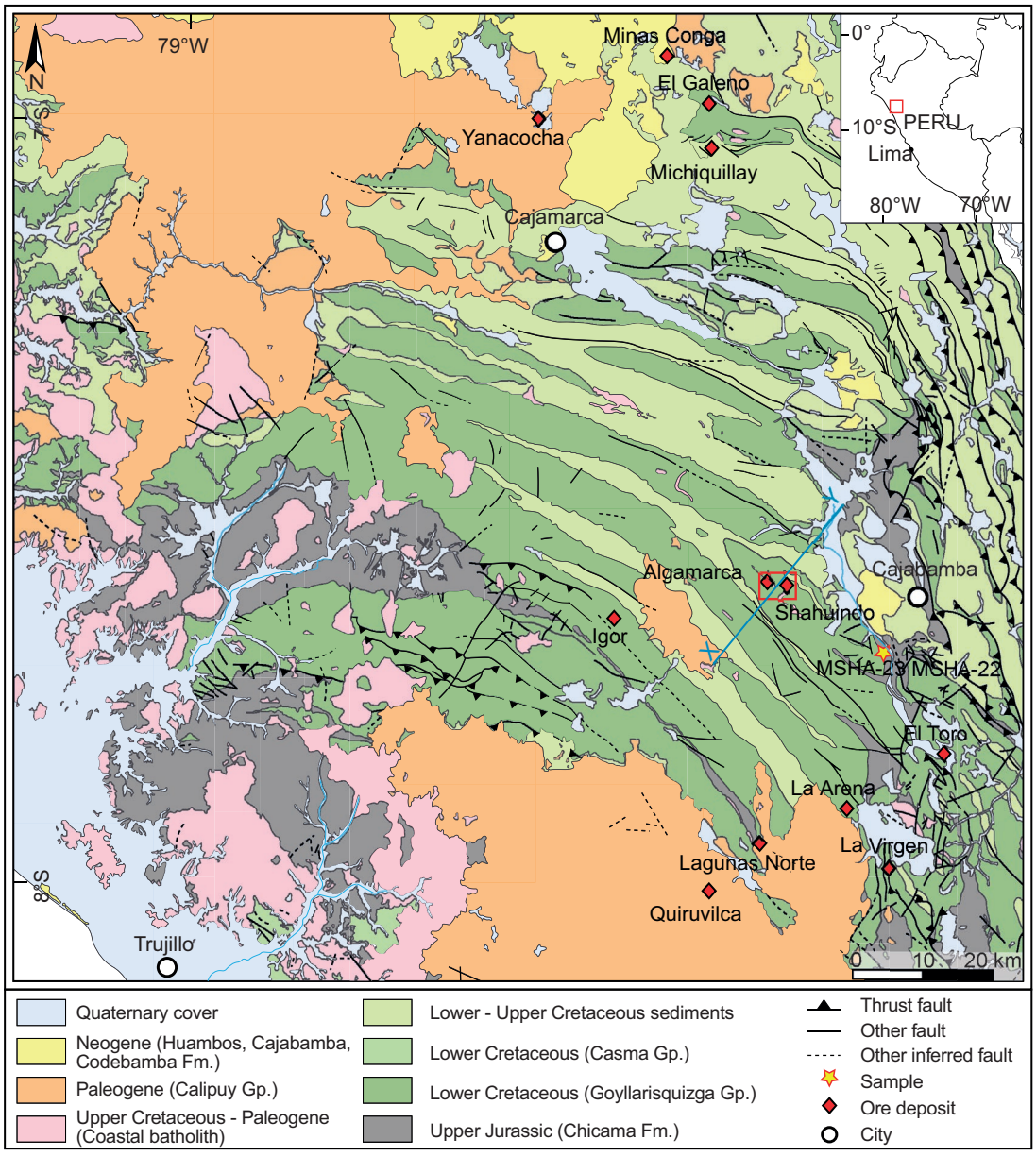

Fig. 1. Geologic map of the Marañón fold-and-thrust belt in northern Peru showing the location of major deposit and projects and the X-Y cross section shown in Figure 4 (modified from Eude, 2014).

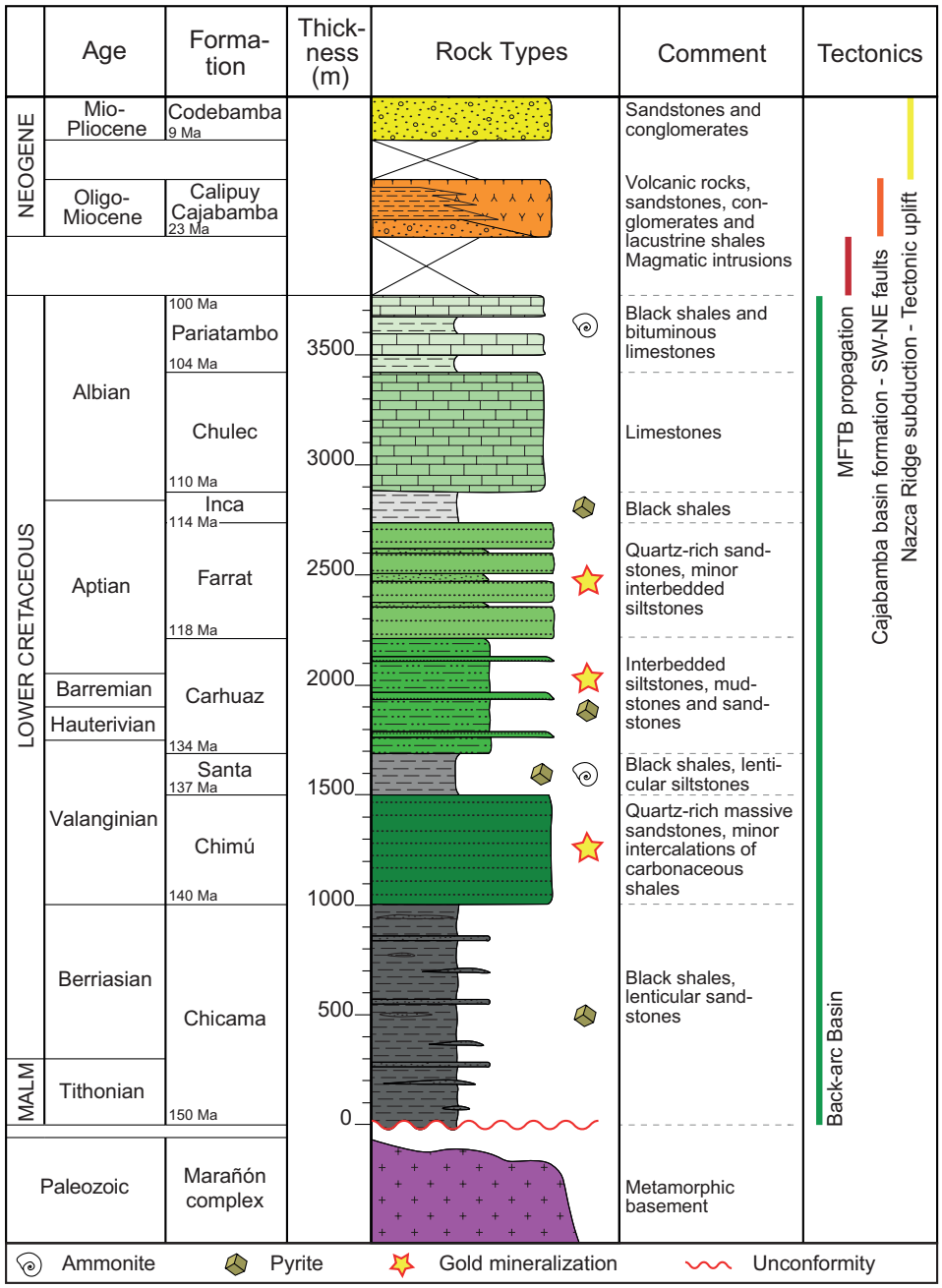

Fig. 2. Stratigraphical column of the Marañón fold-and-thrust belt in the study area (compiled and revised from Jaillard and Jacay, 1989; Defilippi et al., 2012, 2016; Eude, 2014; Prudhomme et al., 2019). MFTB = Marañón fold-and-thrust belt.

Calipuy and Cajabamba basins above the middle Eocene regional unconformity and the intrusion of igneous stocks in the subjacent folded and thrusted Cretaceous sediments (Benavides-Cáceres, 1999; Scherrenberg et al., 2016; Prudhomme et al., 2019; Fig. 1). These relatively weakly deformed basins are associated with normal faulting (Bellier et al., 1989; Prudhomme et al., 2019) and likely have recorded the postorogenic period of tectonic quiescence and relaxation. From the Late Miocene, the Marañón belt and the Calipuy and Cajabamba basins were uplifted and exhumed as a result of the Nazca Ridge subduction (Hampel, 2002; Rosenbaum et al., 2005).

Deposit geology and host-rock lithology

The oldest rocks exposed in the area of the Shahuindo deposit are marine graphite-bearing pyritic shale, silt, and sandstone, with intercalations of coal seams of the Late Jurassic Chicama Formation of ~1,000 m in thickness (Navarro Colque et al., 2010; Figs. 2, 3). The shale and coal layers at the base of the Chicama Formation, at the contact with the Paleozoic basement, are considered to be the detachment plane common to all thrusts in the Marañón belt (Mégard, 1984). The Chicama Formation is overlain by siliciclastic fluvio-deltaic and shallow-marine sequences of the Lower Cretaceous Goyllarisquizga

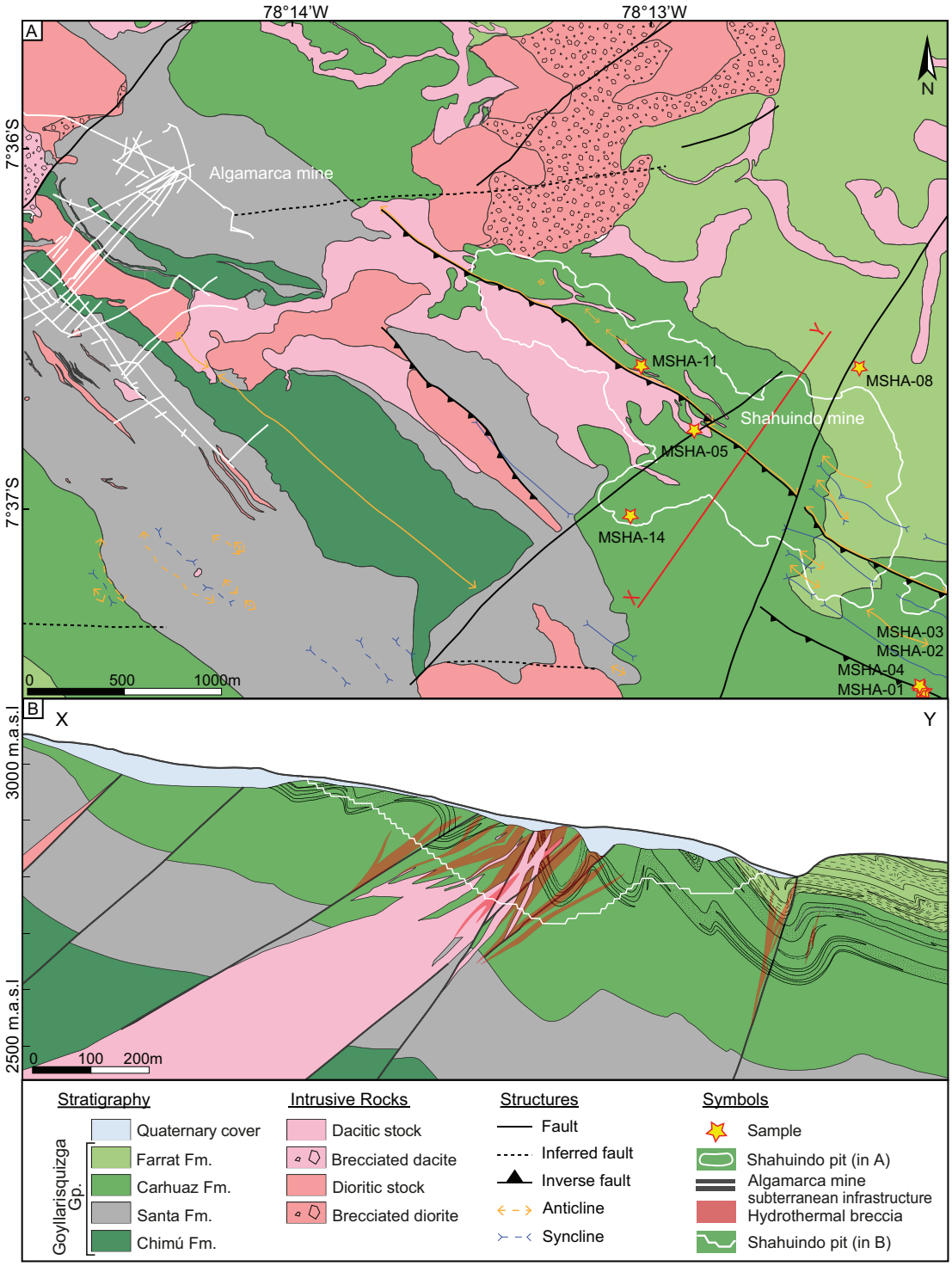

Fig. 3. A. Geologic map of the study area showing the location of the Shahuindo open pit, the former Algamarca mine, and the X-Y cross section shown in B (modified from Defilippi et al., 2016). B. Southwest-northeast cross section of the central part of the Shahuindo deposit (modified from Defilippi et al., 2016). m.a.s.l. = meters above sea level.

Group. The base of the Goyllarisquizga Group comprises ~500 m of fluvial fine- to medium-grained (63–250 and 250–500 μm, respectively) sandstones with occasional coal seams of the Chimú Formation (Jacay, 2005; Navarro Colque et al., 2010). The deposit lithology is described in detail by Defilippi et al. (2016). Briefly, the Chimú Formation forms the core of the Algamarca anticline, which defines the highest elevation of the Shahuindo area (Fig. 3). The Santa Formation lies on the Chimú Formation and is composed of pyritic black shales with local intercalations of limestone. The Santa Formation is strongly deformed and therefore precludes more accurate thickness estimations, which actually range between 150 and

200 m in the mine area. The Santa Formation is covered by ~500 m of gray siltstone interbedded with fine- to medium-grained sandstone, pyritic black shale, and rare bioclastic limestone named the Carhuaz Formation. The uppermost formation of the Goyllarisquizga Group, named the Farrat Formation, is of ~500 m total thickness and includes up to 2-m-thick beds of yellow to white fine- to coarse-grained sandstone and quartzite with minor interbedded siltstone. The Goyllarisquizga sedimentary sequence crops out in the cores of the fault propagation anticlines, northwest-southeast oriented and segmented by northeast-southwest strike-slip and normal faults apparently posterior to the Marañón belt. These northeast-southwest faults segment the Shahuindo deposit into three blocks (western, central, and eastern; see Fig. 3). The eastern and central blocks were down-dropped by hundreds of meters, and the western block is likely to represent the deepest part of the deposit (R.W. Hodder, unpub. report, 2010). Stocks of andesitic (also locally named "diorite porphyry") and later dacitic (or quartz-feldspar porphyry) intrusions of Oligo-Miocene age crop out and are intersected by diamond drilling mostly in the western, deeper part of the deposit (Defilippi et al., 2016). Their emplacement as elongated bodies was generally controlled by anticline axes, thrust faults, and transverse northeast-southwest faults (Fig. 3). Longitudinal fractures in the outer arcs of the hinge zones of the competent unit, like Farrat sandstone, axial planes of anticline (mainly in the San José anticline), thrust faults, transverse faults, intrusion contacts, and permeable layers in sandstone, are all presumably preferred sites for emplacement of mineralization as will be confirmed by the structural analysis in this study (Fig. 4).

Mineralization

The Shahuindo deposit comprises a zone of primary sulfide ore and an oxidized zone of supergene origin. In the latter, gold is found as native metal particles of <5 μm in size, associated with goethite (FeOOH), hematite (Fe_2O_3), jarosite ($KFe_3(SO_4)_2(OH)_6$), and scorodite ($FeAsO_4 \cdot 2H_2O$). Gold reserves in the supergene zone are of 59 t Au at 0.46 g/t, and extraction is currently conducted by heap-leach process (C. Alvarez, pers. commun., 2019). The primary sulfide mineralization does not crop out. Gold reserve estimates for this zone are not currently available, because exploration has not yet been completed. Pyrite is the main sulfide mineral hosting invisible gold in the primary ore, in addition to minor amounts of arsenopyrite, chalcopyrite, galena, sphalerite, tetrahedrite, and stibnite. This assemblage points to an epithermal, so-called intermediate-sulfidation type of deposit for Shahuindo,

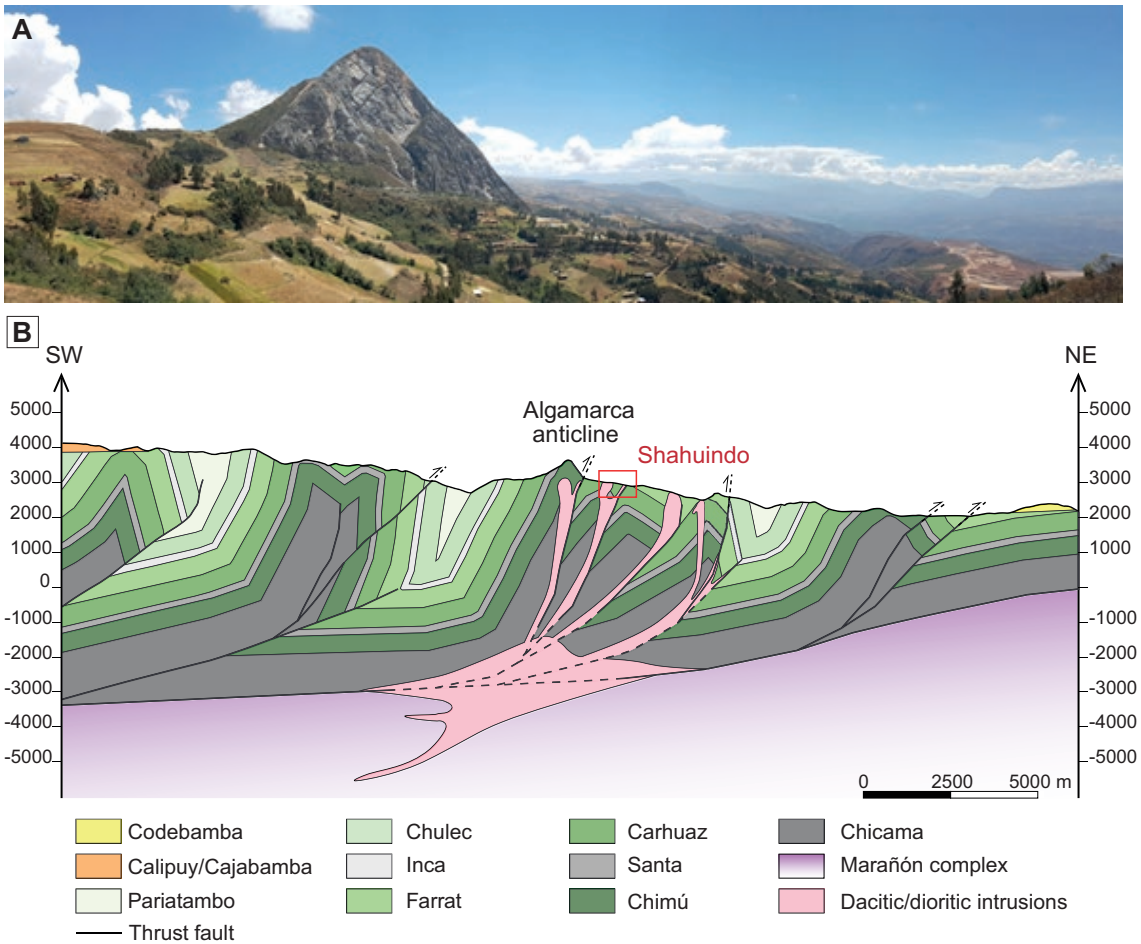

Fig. 4. A. A 2017 view of the Algamarca anticline to the left and the Shahuindo open pit to the right. B. Structural southwest to northeast cross section across the Marañón fold-and-thrust belt reconstructed in this study.

according to Defilippi et al. (2016). Gold grades in the sulfide ore are typically <2 g/t; however, higher grades, up to 33 g/t, were locally measured (R.W. Hodder, unpub. report, 2010; Defilippi et al., 2016). Within the area of endogenic mineralization, the distribution of gold reflects both primary and secondary permeability. The former is induced by favorable sedimentary facies, while the latter occurs because of faults, breccia, and intrusion contacts, with notable paucity of veins and open-space-filling features. In the sedimentary rocks, gold occurs preferentially in the coarse-grained sandstone that is capped by less permeable horizons, and it is hosted within pyrite. Less permeable, graphite-bearing, fine-grained pyrite-rich shale horizons rarely show gold grades in excess of 0.2 g/t, except in the proximity of faults or breccia related to extended fracture networks. In the shale, gold is also spatially associated with pyrite, even though the bulk pyrite content in the rock does not display a direct correlation with gold grades. This can be attributed to the diverse occurrences and origins of pyrite, including fine-grained disseminations of diagenetic origin and/or partial replacement of graphitized vegetal fragments and bioclasts in shale and fine-grained sandstone horizons (Fig. 5A, B), euhedral pyritohedra in medium-grained sandstone (Fig. 5C), bioclast replacement in the rare limestone beds, and filling in <1-cm-thick veinlets (Fig. 5D). Massive coarse-grained pyrite bodies formed locally at the contact between the intrusion and sedimentary host rock are surrounded by a gray-beige silicification halo (Fig. 5E). These pyrite bodies are weakly mineralized, with grades <0.5 g/t Au. The highest gold grades (up to 33 g/t) were found in polyphasic breccia in thrust and transverse faults, within sedimentary rocks.

Multiple porphyritic igneous bodies of andesitic to dacitic composition have intruded the Cretaceous sedimentary rocks in the Shahuindo deposit and the adjacent Algamarca mine area (Fig. 3). Field observations, drill core data, and a preliminary geochronological study (S. Bussey and E. Nelson, unpub. report, 2011, cited by Defilippi et al., 2012) suggest that the oldest intrusions have andesitic composition. Zircon U-Pb dating yielded an age of ~26 Ma, while the youngest dacitic intrusions were dated at ~16 Ma (no error margins reported). In the intrusive rocks, gold mineralization is scarce, only occurring in <5-cm-thick veins and locally in stockworks and breccia cement (Fig. 5F), as well as disseminations in strongly sericitized andesite and dacite. The occurrence of gold in both andesitic and dacitic intrusions provides therefore an upper age limit of 16 Ma for the mineralization at Shahuindo (Defilippi et al., 2016; Vallance et al., 2018; this study). This age is consistent with a K-Ar age value of 15.5 ± 0.4 Ma reported by Noble and McKee (1999) from hydrothermal muscovite bordering a polymetallic vein that crosscuts a quartz monzonite porphyry at Algamarca. These results confirm a value of 16 to 15 Ma for the age of the mineralization at Shahuindo, assuming that both deposits belong to the same magmatic-hydrothermal system.

Methods

Construction of a regional structural cross section

To better understand the stratigraphic and structural architecture of the Marañon fold-and-thrust belt and the tectonic framework of the Shahuindo Au deposit, a regional structural cross section (see Fig. 1 for location) has been constructed following the classic thrust-tectonics concepts (Dahlstrom, 1969; Boyer and Elliott, 1982; Elliott, 1983) and using the structural geology modeling MOVE software (Petroleum Experts, 2022). The structural construction results from the integration of surface data, as structural dips, faults, and stratigraphic contacts in line with the stratigraphic synthesis presented in Figure 2. Surface data were obtained from our own field surveys and 1:100,000 geologic maps available from the Instituto Nacional Geológico, Minero y Metalúrgico del Perú (INGEMMET). In order to validate our construction, the final cross section has been forward modeled based on the MOVE flexural-slip algorithm and assuming constant bed length and thickness. The results are presented in Figure 4.

Analytical techniques

Thirty polished sections from sulfide ore sampled in drill cores were examined using a LEICA DM2500 optical microscope. A selection of key samples was examined on an environmental scanning electron microscope (SEM) Quanta 650 FEI, equipped with an EDAX-Octane Pro energy dispersive spectrometry (EDS) microanalysis system at Centro de Caracterización de Materiales of the Pontifical Catholic University of Peru (CAM-PUCP). Operating conditions were 20-kV accelerating voltage and 5-nA current in backscattered electron (BSE) mode. Bulk contents of carbon, sulfur, other major elements, and a suite of 36 trace elements from 10 host-rock and mineralized samples were determined at ALS Loughrea-Geochemistry, Ireland, and Lima, Peru. Analytical instruments, digestion methods, numerical results, and their corresponding detection limits are given in the Appendix (Table A1).

Major elements (>0.1 wt %) in sulfide minerals were quantified using a CAMECA SXFive electron probe microanalyzer (EPMA) equipped with five wavelength dispersive spectrometers at the Raimond Castaing Microanalysis Centre of the University of Toulouse, France. Analyses were conducted at 25-kV acceleration voltage and 20-nA electron beam current, with a beam diameter of <2 μm and 10 s of counting time at the fluorescence peak and 5 s at the left- and right-side background around the peak. The elements analyzed were S (Kα), As (Lβ), Au (Lα), Fe (Kα), Cu (Kα), and Sb (Lα). Mineral standards included natural chalcopyrite for calibration of Fe, Cu, and S, arsenopyrite for As, and native metals for Au and Sb. The detection limits for each element and the obtained numerical data are reported in Table 1 and Appendix Table A2.

Laser ablation-inductively coupled plasma-mass spectrometry (LA-ICP-MS) analyses of 21 trace elements in sulfide minerals (^{51}V, ^{57}Fe, ^{59}Co, ^{60}Ni, ^{63}Cu, ^{66}Zn, ^{71}Ga, ^{74}Ge, ^{75}As, ^{77}Se, ^{95}Mo, ^{107}Ag, ^{115}In, ^{121}Sb, ^{130}Te, ^{187}Re, ^{189}Os, ^{195}Pt, ^{197}Au, ^{208}Pb, ^{209}Bi) were performed at the GET laboratory using a Thermo Finnigan MAT Element HR quadrupole ICP-MS coupled with a ultraviolet femtosecond laser (New Wave) (energy 0.003 mJ, fluency 0.94 J/cm^2, power 12%, frequency 5 Hz). The laser ablation spot size was ~20 μm for most analyses, with additional spots of ~60 μm for large-grain samples to increase the signal to noise ratio. The counting time for each ablation spot analysis was 140 s, including 30 s of preablation

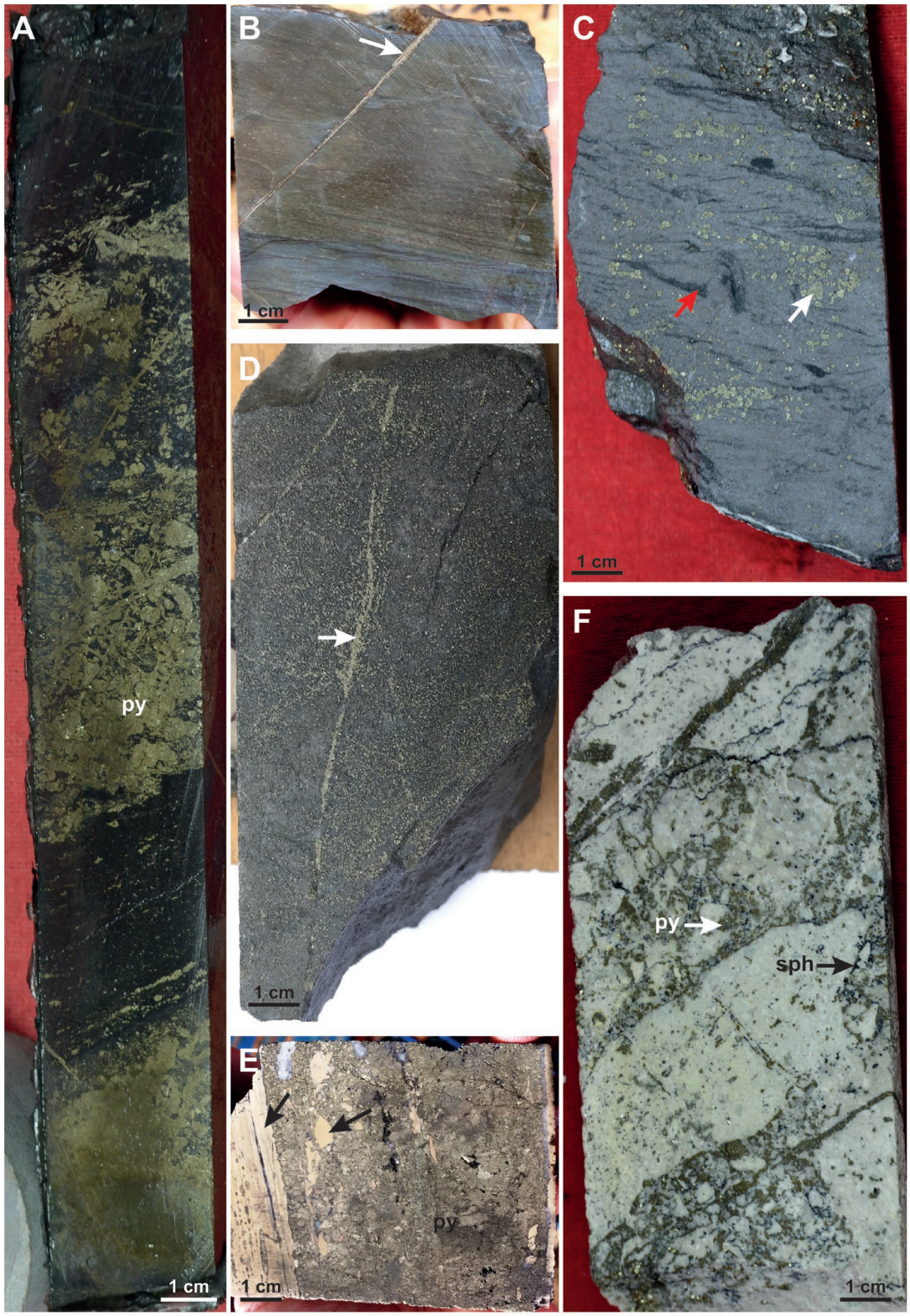

Fig. 5. Photographs of representative samples of the host rocks at the Shahuindo deposit. A. Pyritized vegetal fragments and bioclasts in shale; sample BSHA-05. B. Pyrite (py) I dissemination and late pyII vein (white arrow) in shale; sample MSHA-13. C. Pyrite I overgrown by euhedral coarse-grained pyII (white arrow) in medium-grained sandstone rich in shale clasts (red arrow); sample BSHA-09b. D. Pyrite II dissemination in carbonaceous fine-grained sandstone cut by a pyII-III vein; sample MSHA-08. E. Brecciated and altered medium-grained sandstone (black arrow) cemented by pyII and pyIII; sample MSHA-14. F. Strongly sericitized and brecciated dacite showing abundant pyrite as disseminations (pyII > pyIII), filling veinlets and aggregates in the breccia cement, with local presence of sphalerite (sph); sample BSHA-20.

Table 1. Pyrite and Arsenopyrite Generations, with As and Au Concentration Range and Average Content, for the Shahuindo Mine, as Analyzed by EPMA and LA-ICP-MS

Pyrite / arsenopyrite type	Morphology and spatially associated minerals	EPMA As (wt %) Range **Mean** *Number of points*	LA-ICP-MS Au (ppm) Range **Mean** *Number of points*	Stage
pyI	10- to 200-µm aggregates of subhedral to euhedral cubic microcrysts and framboids; no other sulfides associated	<0.2 **<0.2** *11*	0.1–4.5 **0.3** *56*	Diagenetic/syngenetic
pyII	<2-mm subhedral to euhedral crystals in sandstone, replacing organic detritus and/or bioclasts; dissemination, vein filling, and local breccia cement in intrusions; massive bodies at the contact between igneous intrusions and sedimentary wall rocks; <30-µm pyrrhotite and chalcopyrite inclusions	<0.2–2.4 **0.5** *51*	0.1–9.9 **1.0** *45*	Hydrothermal pre-ore, low As and Au
pyIII	Rims on and/or partial replacement of pyII; massive bodies and breccia cement at the contact between igneous intrusions and sedimentary wall rocks; filling <5-cm-thick veins in dacitic intrusions; oscillatory zoning with As-rich and As-poor bands; in part coeval with arsenopyrite; frequent occurrence of <50-µm inclusions of chalcopyrite, sphalerite, tetrahedrite-tennantite, galena, and stannite	<0.2–5.6 **1.8** *107*	0.1–110.0 **7.0** *129*	Hydrothermal main ore stage, high Au and As
apyIII	Subhedral to euhedral <0.3-mm strongly zoned grains along fracture walls rimmed by pyIII; accompanied by chalcopyrite, sphalerite, tetrahedrite-tennantite, galena, and minor quartz and carbonate	40.9–46.8 **42.3** *23*	1.8–460.0 **55.0** *11*	Hydrothermal main ore stage, high Au and As
pyIV	Only observed in a vein cutting andesitic intrusion and in a contact pyrite body as rims on pyIII; oscillatory zoning with As-rich and As-poor bands; no inclusions observed; accompanied by enargite and minor digenite	<0.2–2.9 **1.8** *12*	0.1–2.6 **0.7** *8*	Hydrothermal late ore stage, medium As and low Au

Abbreviations: EPMA = electron probe microanalysis, LA-ICP-MS = laser ablation-inductively coupled plasma-mass spectrometry

background, 80 s of laser ablation, and 30 s of postablation background. Iron (as ^{57}Fe) was used as the internal standard; its content in arsenian pyrite was determined by EPMA and found to be fairly constant and independent of As content (±0.1 wt %). The external calibration reference materials were Po-726 (Sylvester et al., 2005), NIST610 (Norman et al., 1996), MASS-1 (Wilson et al., 2002), and a natural arsenopyrite (Pokrovski et al., 2002, 2021).

Thermodynamic modeling of fluid-rock interactions

Chemical speciation and mineral solubility in simplified fluid-rock systems relevant to the geologic context of the deposit were modeled using available robust thermodynamic data. The goal was to better constrain the major compositional fluid and ore-forming parameters to help validate the proposed model of formation. In particular, the major focus in this study was on evaluating the role of organic matter on Fe, Au, and As transport and precipitation. Other accompanying trace elements were not considered in detail by the modeling, because of the paucity of both analytical and thermodynamic data on their content, distribution, and speciation in the fluid and major host ore mineral (pyrite).

Calculations were performed using the HCh software package and associated Unitherm database, allowing chemical equilibrium simulations in multicomponent fluid-mineral systems based on the minimization of the Gibbs energy of the system (Shvarov, 2008, 2015), and accounting for nonideality of the fluid using the extended Debye-Hückel equation (Helgeson et al., 1981). The selection of thermodynamic data sources and their consistency for Au, S, and Fe were discussed in detail elsewhere (Pokrovski et al., 2015, 2019, 2022a, b; Kokh et al., 2016, 2017) and are only briefly overviewed here. The thermodynamic properties of the minerals were taken from the Joint Army-Navy-Air Force (JANAF; Chase, 1998) and the U.S. Geological Survey (USGS; Robie and Hemingway, 1995) databases, whereas major fluid components (salts) and most sulfur aqueous species were adopted from the updated SUPCRT database (Johnson et al., 1992) or its recently extended equivalent, SUPCRTBL (Zimmer et al., 2016) and were complemented by recent data for important ionic sulfur forms including S_3^- (Pokrovski and Dubessy, 2015) using the revised and extended Helgeson-Kirkham-Flowers equation of state (HKF; Oelkers et al., 2009; Sverjensky et al., 2014; references therein). A large set of organic aqueous ions and molecules (hydrocarbons, carboxylic acids, thiols) whose thermodynamic coefficients are available in the SUPCRT database was also tested in the calculations, but their equilibrium concentrations were found to be too low (<0.001 m, where m is number of moles per kg of water) to significantly affect the fluid properties (pH, redox) and mineral solubility, compared to the dominant CO_2 and CH_4. The data for ferrous iron species (Fe^{2+}, $FeCl^+$, and $FeCl_2^0$) were taken from the SUPCRT database, whereas those for $FeCl_4^{2-}$ from Testemale et al. (2009). Both $FeCl_2^0$ and $FeCl_4^{2-}$ dominantly contribute to

the Fe speciation at our conditions. The properties of aqueous As^{III} and As^{V} oxyhydroxide complexes and iron (sulfo)arsenide minerals (FeAsS, $FeAs_2$, and FeAs) were adopted from Perfetti et al. (2008). The major arsenic aqueous species over the entire range of our conditions is arsenious acid, $As(OH)_3^0$. We also incorporated and examined the recent model of As solid solutions in marcasite and arsenopyrite recently proposed by Xing et al. (2019) based on the data for those pure phases from Perfetti et al. (2008) and density functional theory and Monte Carlo theoretical calculations of As substitution for S in the FeS_2 and FeAsS structures by Reich and Becker (2006). This model yielded As tenors in pyrite (0.5–1.0 wt %) right in the middle of the analyzed range of our samples and thus was judged to be adequate to account for the general arsenic distribution and mass balance between fluid and rock. The thermodynamic properties of the molecular sulfur aqueous forms, H_2S, SO_2, and dissolved H_2, O_2, CO_2 and CH_4, were adopted according to the Akinfiev and Diamond (2003) model for aqueous nonelectrolytes, which allows a more accurate description than the HKF model over the T-P range relevant to our study (<350°C; <1 kbar; Pokrovski and Dubessy, 2015). Note that the thermodynamic data from Akinfiev and Diamond (2003) have also been used in derivation of the thermodynamic properties of the Au species and thus were chosen here to maintain thermodynamic consistency. The thermodynamic properties of traditional hydrogen sulfide ($AuHS^0$, $Au(HS)_2^-$) and hydroxide ($AuOH^0$) species were taken from the compilation of Pokrovski et al. (2014), consistent with existing robust experimental data (e.g., Stefansson and Seward, 2004; Tagirov et al., 2005), whereas those for the dichloride species ($AuCl_2^-$) were taken from Zotov et al. (2018) and those for the recently discovered gold complex with the trisulfur ion, $Au(HS)S_3^-$, from Pokrovski et al. (2015). Species such as $AuCl^0$, $AuCl_3^-$, and $Au(OH)_2^-$, tentatively suggested in some previous compilations, were ignored in the present modeling because of the large uncertainties associated with predictions of their stability constants at elevated temperatures as well as the lack of direct spectroscopic evidence of their existence. Among the chosen Au species, $AuHS^0$ and $Au(HS)_2^-$ are the dominant complexes at acidic (<4) and neutral to basic pH (>6), respectively, in the S-bearing epithermal fluids considered in this study (e.g., Tagirov et al., 2005). In addition, $Au(HS)S_3^-$ also contributes to the gold solubility at intermediate pH values (4–5) at redox conditions of the sulfate-sulfide coexistence in the fluid. The precision of our predictions of Au, Fe, and As concentrations at a given model fluid composition at the T-P conditions of this study (150°–350°C, <1,000 bar) is typically better than 50% of the concentration value, as conditioned by the intrinsic uncertainties of the thermodynamic data and activity coefficient models chosen here. The input HCh files of representative models are supplied as an electronic supplement (App. 1).

Results

Structural analysis

The structural framework, reconstructed in this study, is illustrated by the regional structural cross section in Figure 4. It shows the geometry of the imbricated thrusts and associated folds of the E-verging Marañón belt, which has been partly eroded during the middle Eocene postorogenic period (Noble et al., 1990; Prudhomme et al., 2019). The belt is covered to the west by the Calipuy volcaniclastic sediments and to the east by the Codebamba lacustrine and fluvial deposits (Figs. 2, 4). Both formations are poorly deformed, indicating that the Neogene reactivations of thrusts structures were rather weak. Imbricated thrusts and folds are tight and accommodated a large degree of shortening. They are connected to a sole thrust that developed at the interface between the Chicama black shales and the metamorphic basement. The entire thickness of the Chicama black shales (~1,000 m) was deformed, and the shales occupy the cores of imbricates and anticlines, which form excellent structural traps when preserved. The Chicama base décollement developed between 7 km deep in the west and 2 km in the east, with a steep slope in the east.

Our structural analysis shows that the Shahuindo deposit is located in a system of four imbricate thrusts where the related anticlines are preserved. The most spectacular of these anticlines is the Algamarca anticline, which marks the landscape of the region with an outcropping fold made of Chimú sandstones (Fig. 4). The Algamarca imbricate is the most western and uplifted and thus the first to have been formed in accordance with the in-sequence thrusting propagation evidenced by the normal stacking of the four imbricates. The Shahuindo gold deposit has been trapped in the reservoir sandstones (Carhuaz and Farrat Formations) of the anticlines of the second and third imbricates. It is possible that similar deposits could also exist in the Chimú sandstones, but these have not yet been revealed by the mine drill holes. In the Algamarca-Shahuindo imbricate system, elongated bodies of andesitic and dacitic intrusions are emplaced at the intersection of the northwest-southeast thrust faults and later northeast-southwest transverse faults. In our structural interpretation, these intrusions are connected to an upper crustal laccolith installed at the interface between the basement and the Chicama black shales, following the model of Vigneresse et al. (1999) and Richards (2003), and resulting from magma migration along deeper and later northeast-southwest transverse faults clearly identified at the surface (Fig. 3). As a result of this analysis, the obtained structural cross section allows us to circumscribe the Algamarca-Shahuindo imbricate system that likely fed the Shahuindo deposit. The migration of ore fluids was guided by the thrust geometries up to the reservoir sandstones of the anticlines, showing analogies with processes typically observed in petroleum systems (e.g., Magoon and Dow, 1994; Calderon et al., 2017; Baby et al., 2021). Moreover, the Lower Cretaceous Shahuindo stratigraphic series comprise essential elements as black shales, sandstone reservoirs, and overburden rocks (Fig. 2) that all contributed to the processes of trap formation and fluid migration and accumulation linked to thrust tectonics of the Marañón belt.

Host-rock and ore geochemistry

Thirty-seven samples were collected in the Shahuindo area, most of them (n = 32) selected from drill core to avoid the influence of supergene alteration. Barren and gold-rich samples were collected from both sedimentary and igneous rock types of the Shahuindo area in order to characterize all facies of the deposit. Additionally, two fresh outcrop samples

of graphite-bearing sandstone from the Chicama Formation were collected about 20 km southeast of the deposit, where no igneous and/or hydrothermal activity was detected, to assess the host rock unaffected by hydrothermal fluids. The location of the 10 samples from mineralized and barren sedimentary rocks as well as their mineralogical and geochemical characteristics are given in Figures 1 and 3, Appendix Figure A1A, Tables 2 and 3, and Appendix Table A1. Locations of graphite-rich sandstone samples from the Chicama Formation (MSHA-22 and MSHA-23) are shown in Figure 1. The Chimú Formation was not sampled, because it was not intersected by exploration drilling, and all exposed occurrences are affected by strong supergene alteration. The Santa Formation was sampled from core drilled in the deposit (MSHA-05). The Carhuaz Formation was sampled from surface outcrops (samples MSHA-01 to MSHA-04; Fig. 3A) as well as from drill core (MSHA-08; MSHA-11). Sample MSHA-14 is from a breccia with pyrite cement at the contact between a dacitic intrusion and fine-grained sandstone of the Carhuaz Formation (Fig. 5E).

Based on their chemical and mineralogical compositions, the rock samples were separated into two groups. The first consists of three barren samples, including MSHA-22 and MSHA-23 from outside the deposit and MSHA-01 collected within the deposit. They do not show any Au, As, or Cu enrichment compared to typical black shales (Johnson et al., 2017). These samples have major element compositions within the range of typical barren black shales (Johnson et al., 2017; App. Fig. A1). Their gold and arsenic contents (<1–2 ppb and 12–23 ppm, respectively) are at the lower end of the range of

Table 2. Description and Key Element Bulk Composition of Selected Rock Samples from the Shahuindo Mine

Sample identity	Sample type and location	Geographical coordinates	Description	C (wt %)	S (wt %)	Fe[1] (wt %)	Cu (ppm)	As (ppm)	Au (ppm)
MSHA-01	Surface outcrop	7°37'30.02"S 78°12'19.04"W	Carhuaz Formation; light-gray siltstone with flaser bedding; black organic matter accompanied by fine-grained pyrite is abundant in mud layers	0.43	0.22	5.31	30	12	0.002
MSHA-02	Surface outcrop	7°37'30.14"S 78°12'18.31"W	Carhuaz Formation; light-gray siltstone with flaser bedding; black organic matter accompanied by fine-grained pyrite is abundant in mud layers	0.94	0.44	3.84	130	16	0.02
MSHA-03	Surface outcrop	7°37'30.14"S 78°12'18.31"W	Carhuaz Formation: light-gray siltstone with flaser bedding; black organic matter accompanied by fine-grained pyrite is abundant in mud layers	0.93	0.53	4.15	124	21	0.02
MSHA-04	Surface outcrop	7°37'29.27"S 78°12'19.60"W	Carhuaz Formation, SW-NE fault zone; strongly deformed black shale accompanied by coarse-grained pyrite	0.13	7.15	6.81	31	743	0.18
MSHA-05	Drill core within the deposit	7°36'35.94"S 78°12'53.54"W	Santa Formation; black shale rich in carbonaceous material with dissemination of fine-grained pyrite	0.65	0.75	3.74	37	41	0.03
MSHA-08	Drill core within the deposit	7°36'23.52"S 78°12'27.80"W	Fine-grained dark-gray sandstone of the Carhuaz Formation; dissemination of abundant subidiomorphic pyrite (>0.5 mm); yellow fine-grained pyrite fills sinuous veinlets (<1 mm)	0.03	19.3	16.71	8250	1,000	0.95
MSHA-11	Drill core within the deposit	7°36'24.39"S 78°13'01.73"W	Fine-grained dark-gray sandstone of the Carhuaz Formation with abundant carbonaceous matter including plants fragments and dissemination of fine-grained pyrite	1.43	5.09	4.70	64	237	0.03
MSHA-14	Drill core within the deposit	7°36'49.36"S 78°13'02.87"W	Matrix-supported breccia with ~30% subangular to subrounded clasts of altered medium-grained sandstone; the cement is mainly pyrite with minor amounts of arsenopyrite, tetrahedrite-tennantite, Bi and Te minerals, aluminum phosphate-sulfate minerals, and quartz; sample collected at a sandstone/intrusion contact	0.20	21.9	18.81	57	2,460	0.25
MSHA-22	Surface outcrop 20 km SE of the deposit	7°41'39"S 78°05'07"W	Chicama Formation; light-gray fine-grained sandstone with flaser bedding; black organic matter accompanied by fine-grained pyrite is abundant in mud layers; left side of the Rio Condebamba River	1.91	0.44	2.78	21	12	0.001
MSHA-23	Surface outcrop 20 km SE of the deposit	7°41'39"S 78°05'07"W	Chicama Formation; light-gray fine-grained sandstone with flaser bedding; black organic matter accompanied by fine-grained pyrite is abundant in mud layers; left side of the Rio Condebamba River	2.27	0.37	3.35	26	23	<0.001

[1]Calculated on the basis of the oxide analysis; see also Appendix Table A1

Table 3. Comparison of Element Content Along a 50-m-Long Profile Perpendicular to a Roof Branch of the Thrust that Controls Mineralization at the Deposit Scale

Sample	Location	Au (ppb)	As (ppm)	Ag (ppm)	S (wt %)	Fe excess[1] (mol/kg)
MSHA-01	50 m SW of the thrust	2	12	0.1	0.22	0.09
MSHA-02	25 m SW of the thrust	17	16	0.1	0.44	0.06
MSHA-03	25 m SW of the thrust	17	21	0.2	0.53	0.06
MSHA-04	0 m from the thrust	180	743	0.7	7.15	0.01

[1]Fe excess, in moles per 1 kg of rock, relative to the FeS_2 stoichiometry, that all S is in pyrite

whole-rock analyses of black shales compiled for the Sukhoi Log, Carlin, and Bendigo Au-As provinces (Large et al., 2011). Mass balance calculations, assuming all sulfur to be in pyrite, show iron to be in excess compared to sulfur (i.e., mole ratio Fe/S > 0.5; App. Fig. A1B) for samples that contain less than 1 wt % S, thereby suggesting an additional contribution from other Fe-bearing minerals (silicates, carbonates). In contrast, hydrothermal pyrite-bearing samples enriched in gold (0.02–1.0 ppm) show a mole Fe/S ratio close to 0.5 (App. Fig. A1C), indicating that almost all of the iron and sulfur are hosted by pyrite. Assuming all carbon to be from carbonaceous matter (traces of carbonate were only found in sample MSHA-14), there is no correlation between carbonaceous matter contents and gold concentrations. Samples MSHA-02, MSHA-03, and MSHA-04 belong to the above-mentioned 50-m-long profile starting with MSHA-01 (Fig. 3A). While samples MSHA-02 and MSHA-03 do not differ in mineralogy and texture from sample MSHA-01 (Table 3), they show significantly higher Au, S, and As concentrations and much smaller Fe excess. These compositional differences are even more pronounced in sample MSHA-04 taken from the fault zone itself.

Pyrite paragenetic sequence

Pyrite is by far the major sulfide mineral associated with gold at Shahuindo, accompanied by subordinate amounts of arsenopyrite, pyrrhotite, chalcopyrite, sphalerite, tetrahedrite-tennantite, enargite, chalcocite, and galena and minor stibnite, bismuthinite, tellurobismuthite, kobellite, stannite, boulangerite, and greenockite. Gangue minerals comprise, in decreasing abundance, white micas, quartz, kaolinite, carbonates, pyrophyllite, and aluminum phosphate-sulfate minerals. In contrast to samples affected by oxidation from the supergene zone (the defined gold resource), in the endogenous sulfide ore no visible gold was detected by optical microscopy nor SEM, even in samples with grades as high as 30 g/t Au. Figure 6 shows the paragenetic sequence comprising four successive stages as defined by four generations of pyrite identified in this study based on morphological characteristics, chemical composition, and mineral assemblages as summarized in Table 1 and detailed below.

Pyrite I: The earliest pyrite (pyI) occurs as aggregates of subhedral to euhedral cubic-shaped microcrysts and framboids of 10 to 200 μm in size, which are only observed in the

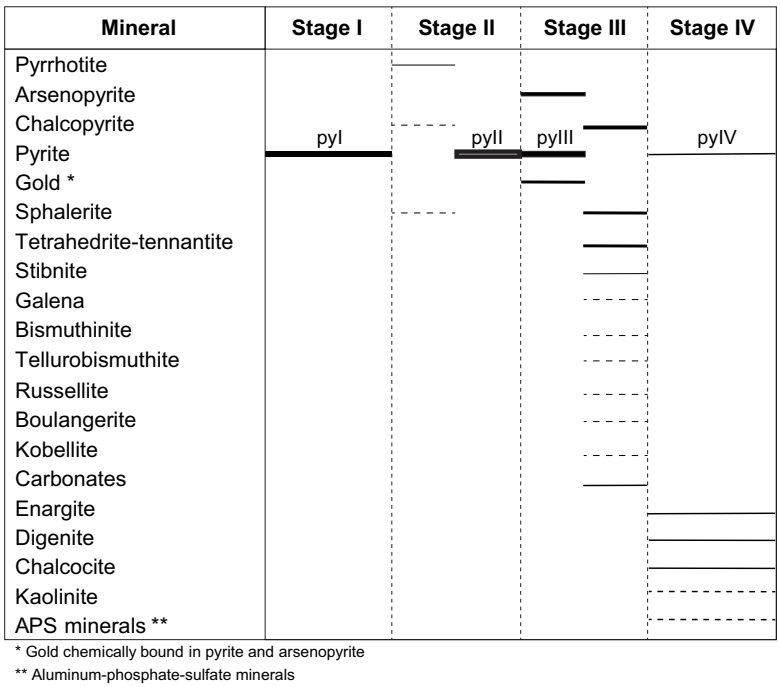

Fig. 6. Paragenetic sequence of the Shahuindo gold deposit as established in this study. The bar thickness is roughly indicative of the relative mineral abundance. Stage I corresponds to the deposition of diagenetic pyI; pyrrhotite, chalcopyrite, and sphalerite of stage II occur as inclusions within coarse-grained pyII; gold precipitated within pyIII and arsenopyrite during stage III, and the other sulfides fill open space between their euhedral terminations, with evidence of local replacement; pyrite IV forms overgrowths on pyIII and is accompanied by enargite, minor digenite, and aluminum phosphate-sulfate minerals, partially replacing stage III chalcopyrite and tetrahedrite-tennantite.

sedimentary rocks of the Santa and Carhuaz Formations (Fig. 7A, B). This pyrite type is not accompanied by other sulfide minerals and occurs as disseminations at a regional scale, strongly suggesting a diagenetic origin.

Pyrite II: Stage II pyrite (pyII) is the most abundant of the four types. It is spatially associated with intrusive bodies and occurs both in the igneous rocks and nearby sediments. Pyrite II occurs mainly as pyritohedral crystals up to 5 mm in size, filling porosity in sandstone, (Fig. 6C-E), replacing organic detritus and/or bioclasts in siltstone and shales (Fig. 6F), or filling veinlets. Pyrite II is also the main constituent of pyrite bodies formed at the contact between igneous intrusions and sedimentary wall rocks. In the igneous rocks, disseminated pyII occurs together with sericite as replacement of mafic minerals. It also fills thin veinlets (<5 mm thick) that are locally interconnected and form a stockwork array and is an important constituent of the breccia matrix. In both igneous and sedimentary rocks, SEM analyses do not show compositional zoning of pyII (Fig. 6E) but reveal the presence of <30-μm-size inclusions of pyrrhotite and, less commonly,

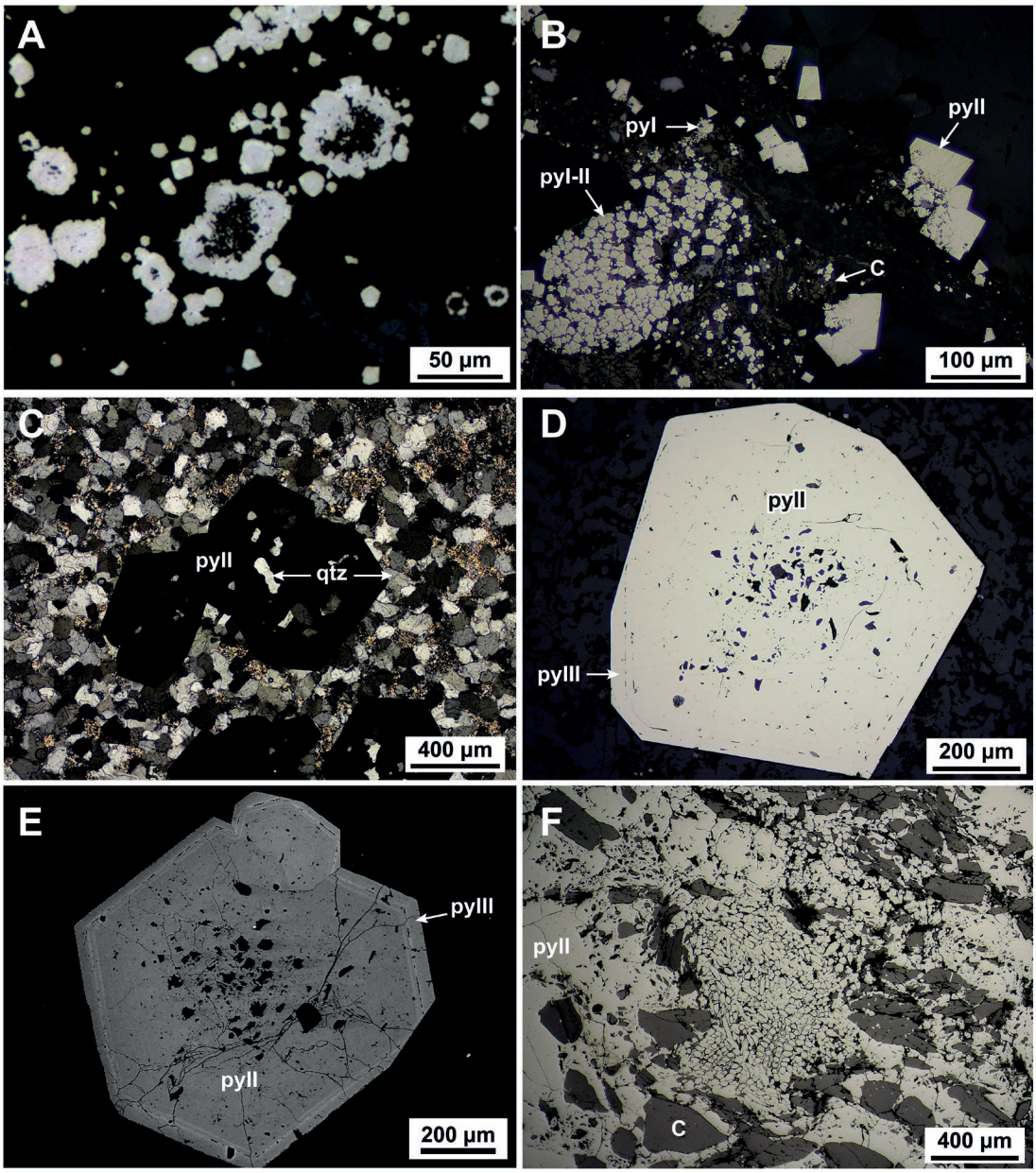

Fig. 7. Textural features of pyrite I and pyrite II from the Shahuindo deposit. A. Cluster of subhedral to euhedral pyrite microcrysts. Reflected light. B. Spatial association between framboidal pyrite (pyI) and graphitic organic detritus (C). Pyrite II (pyII) nucleation on pyrite I, making it difficult to distinguish between pyI and pyII. Reflected light. C. Subhedral pyritohedron (py) in sandstone that encloses detrital quartz (qtz). Transmitted light, crossed polars. D. Euhedral pyrite II grain with As-rich pyrite III (pyIII) overgrowths. E. Backscattered electron image of coarse euhedral pyrite II grain with pyrite III overgrowths showing alternating As-rich (lighter color) and As-poor bands. F. Partial replacement of graphitic organic detritus (C) by pyrite II (pyII), locally infilling plant cells (center of the picture). Reflected light.

intergrowths of pyrrhotite, chalcopyrite, and sphalerite with local chalcopyrite disease.

Pyrite III: Similar to pyrite II, pyrite III (pyIII) was observed both in sedimentary and igneous rocks as well as in massive pyrite bodies. Pyrite III typically forms rims on pyII (Fig. 6E) and, less frequently, fracture and crystallographically controlled replacement zones (Fig. 7A). The key distinguishing feature of pyIII is an oscillatory zoning with an alternation of As-rich and As-poor bands (Fig. 7B, D). As-rich bands often contain <50-μm inclusions of chalcopyrite, sphalerite, tetrahedrite-tennantite, galena, and stannite (Fig. 7D) and, more rarely, bismuthinite, tellurobismuthite, kobellite, and russellite. Arsenopyrite (apyIII) is coeval with pyIII and forms strongly zoned subhedral to euhedral grains (<0.3 mm; Fig. 7B, C, E). Locally, arsenopyrite occurs as euhedral crystals along fracture walls rimmed by pyIII within pyII (Fig. 6B, E). In these fractures, chalcopyrite, sphalerite, tetrahedrite-tennantite, galena, and minor quartz and carbonate fill open space between euhedral terminations with evidence of local replacement (Fig. 7E).

Pyrite IV: The fourth generation of pyrite (pyIV) was only identified in a vein cutting an andesitic porphyry body and in a massive pyrite contact body. Pyrite IV occurs as inclusion-free overgrowths on pyIII with alternation of As-rich and As-poor bands (Fig. 7F), and is accompanied by enargite, minor digenite, and aluminum phosphate-sulfate minerals, partially replacing chalcopyrite and tetrahedrite-tennantite.

Pyrite and arsenopyrite composition

The EPMA analyses of pyrite I show a close to ideal stoichiometry, $FeS_{2.00}$, and no As, Sb, and Cu were detected (<0.05–0.1 wt %; Fig. 8; App. Table A2). Pyrite II is also close to stoichiometric ($FeS_{1.98–2.00}$), with detectable As (up to 2.4 wt %). Pyrite III is more enriched in both As and Cu (up to ~5.6 and ~0.9 wt %, respectively). The latest pyrite type, pyrite IV, contains up to 2.9 wt % As. There are no significant correlations between S and As in pyII, whereas in pyIII and pyIV both elements display negative correlations (Fig. 9A), implying an isomorphic substitution by As in the –I formal oxidation state for S in the pyrite structure (e.g., Fleet and Mumin, 1997; Simon et al., 1999; Deditius et al., 2008; Manceau et al., 2020; references therein). The strongest As enrichment in pyIII was observed in grains hosted by sedimentary rocks, whereas the lowest concentrations were found in grains occurring in transverse faults (Fig. 9B). Arsenopyrite, belonging to the pyIII stage, is generally depleted in As ($Fe_{0.98–1.01}As_{0.85–1.00}S_{1.13–1.00}$) compared to the ideal FeAsS stoichiometry, and it is zoned, with cores having lower As (~41 wt %) than the rims (~47 wt %). Sulfur correlates negatively with As plus Sb supporting an (As + Sb) to S substitution mechanism, typical of most arsenopyrites (e.g., Boiron et al., 1989; Pokrovski et al., 2021).

Trace element composition of pyrite and arsenopyrite

Pyrite (from the four paragenetic stages; Fig. 6) and arsenopyrite (from the pyIII stage) were analyzed for trace elements using LA-ICP-MS in 10 representative samples collected in sandstone, andesite, contact sedimentary rocks/dacitic bodies, dacitic bodies, and the northeast-southwest fault (Fig. 10; Table 4; App. Tables A3, A4). Gold contents in pyI range from 0.1 to 1.7 ppm (with a single data point of 4.5 ppm). Gold correlates positively with Ge, Se, and Te and negatively with V, Ga, and In but shows no statistically meaningful pattern with As (Fig. 11A). In pyII, gold ranges from 0.03 to 9.9 ppm (mean value ~1 ppm) with a generally positive correlation with As, depending on the host lithology (App. Table A4). Gold concentrations in pyIII range from ~0.1 to 110 ppm, with the highest concentrations measured in pyrite bodies at the contact of dacitic intrusions with the sedimentary rocks (Fig. 11B). Conversely, the lowest values were observed in pyrite from the andesitic intrusion. The correlations between gold and other elements in pyIII vary greatly depending on the host lithology. Gold and arsenic are strongly correlated in pyrite samples from transverse faults and intrusions but uncorrelated in pyrite from samples from sedimentary rocks. Other minor/trace elements such as Ni, Cu, Zn, Ag, In, Sb, Te, Pb, and Bi locally show relatively high tenors and often strong intercorrelations (App. Fig. A2; App. Tables A2, A4). Such correlations suggest that some spot analyses may include microparticles of minerals like chalcopyrite, kobellite, or tetrahedrite-tennantite. Indeed, the presence of such mineral inclusions is confirmed by SEM analyses (see Fig. 7D-F) as well as by observation of spikes in some laser ablation spectra of pyrite. The presence of arsenic-rich mineral phases (such as tetrahedrite-tennantite) that do not contain significant gold (e.g., George et al., 2017) would, at least partly, obscure correlations between As and Au in sediment-hosted pyIII samples. Gold in arsenopyrite from the pyIII generation exhibits a large range of concentrations (2–460 ppm) independent of the lithology (Fig. 11C, D; App. Table A3). LA-ICP-MS signals of Cu, Zn, Ag, Ga, Ge, Sb, and In in arsenopyrite often show spikes and/or irregular patterns, which are suggestive of the presence of tetrahedrite-tennantite and/or chalcopyrite inclusions enriched in those elements (App. Fig. A3). This interpretation is in accordance with the textures of pyIII and apyIII indicating replacement by these Cu-bearing minerals. Pyrites III and IV show similar alternation of As-rich and As-poor zones, but pyIV is almost free of inclusions and has a lower average content of trace elements than pyIII (Fig. 10; Table 3). Gold concentrations in pyIV range from 0.1 to 2.6 ppm (mean = 0.7 ppm), weakly correlating with arsenic.

Discussion

Evolution of the ore-forming conditions and succession of the mineralization events

The structural reconstruction analysis and the paragenetic sequence established above provide key constraints on the evolution of ore-forming conditions during the Shahuindo deposit formation. The earliest ore mineral assemblage, identified both in sedimentary and intrusive rocks, is only evidenced by residual inclusions of pyrrhotite, chalcopyrite, and sphalerite within the abundant pyII mineralization. This assemblage is consistent with deposition under relatively reducing and sulfur-poor conditions, indicative of pyrrhotite stability. Extensive hydrothermal alteration of the intrusions that accompanies pyII deposition suggests acidic pH conditions, as sericitization is typically associated with percolation of acidic fluids (Hemley and Jones, 1964; Hemley and Hunt, 1992; Seedorff et al., 2005). The occurrence, in the following

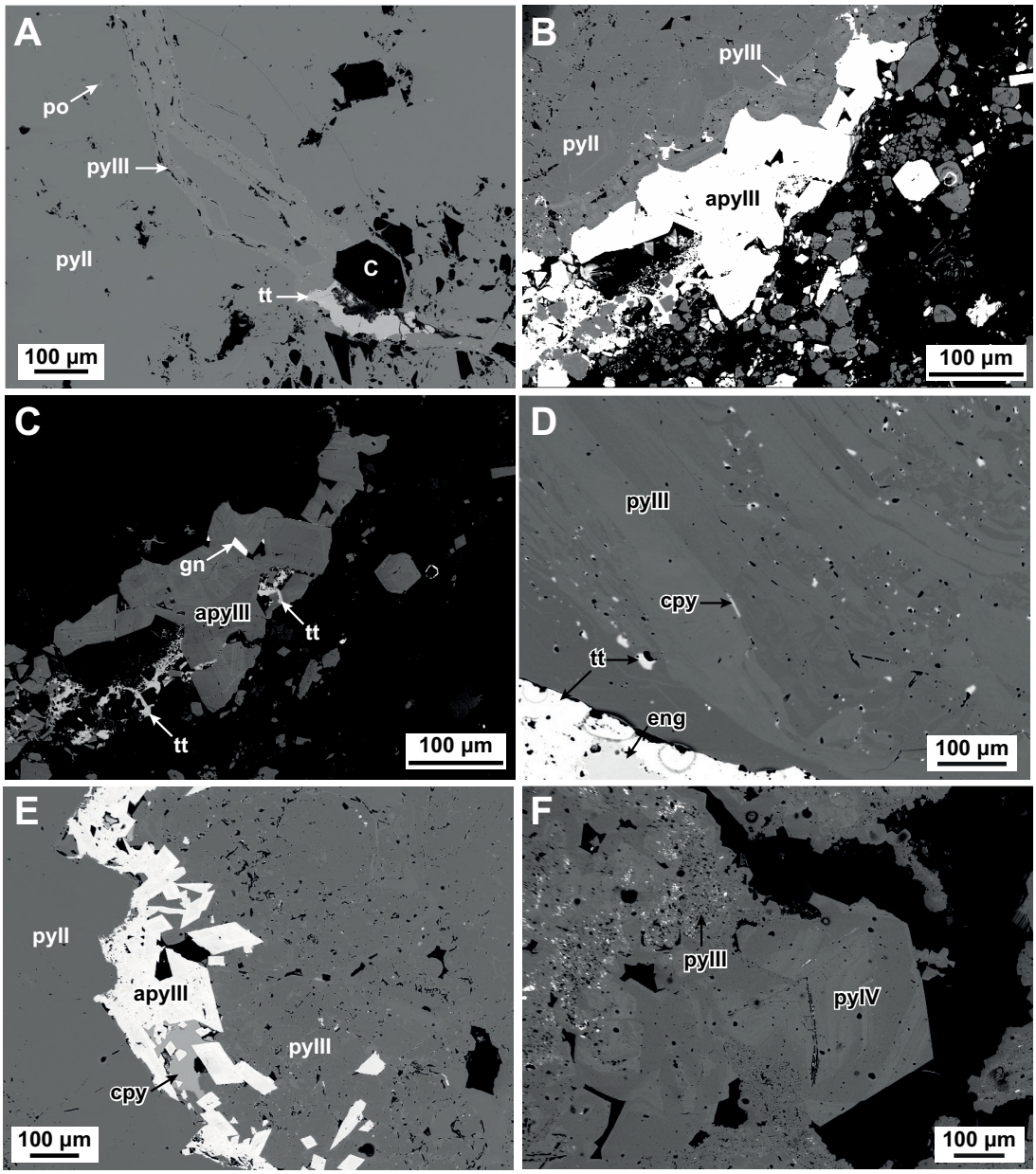

Fig. 8. Scanning electron microscope (SEM) photomicrographs (in backscattered electron mode) of ore samples from the Shahuindo deposit. A. Replacement zone of pyrite II (pyII) by pyrite III (pyIII) and tetrahedrite-tennantite (tt). C = graphite, po = pyrrhotite inclusion in pyrite II. B. Pyrite II (pyII) rimmed by oscillatory-zoned pyrite III (pyIII) and arsenopyrite (apyIII). C. Same view as in B, with different contrast enhancing the arsenopyrite zoning and the later tetrahedrite-tennantite (tt) and galena (gn). D. Details of the oscillatory zoning in pyrite III (pyIII); tetrahedrite-tennantite (tt) and chalcopyrite (cpy) inclusions are preferentially located at the limit between bands; later enargite (eng) partially replacing tetrahedrite-tennantite. E. Arsenopyrite (apyIII) precipitated at the contact between coarse pyrite II (pyII) and finer pyrite III (pyIII) grains with local replacement of the latter; chalcopyrite (cpy) filling spaces between arsenopyrite euhedral terminations. F. Late subhedral oscillatory-zoned and inclusion-free pyrite IV (pyIV) occurring as overgrowth on oscillatory-zoned inclusion-bearing pyrite III (pyIII).

pyIII stage, of Au-rich highly arsenian pyIII and arsenopyrite with the presence of later Ca-Mg-Fe carbonate minerals indicates less acidic fluid pH, more favorable for stabilizing the carbonate mineral phases. The chalcopyrite-tetrahedrite-tennantite assemblage that postdates Au-bearing pyIII and arsenopyrite points to an evolution toward higher sulfidation conditions, as also suggested by late pyIV together with digenite, enargite, kaolinite, and aluminum phosphate-sulfate minerals within the magmatic intrusions and at their contacts with sedimentary rocks (Einaudi et al., 2003; Fontboté et al., 2017). This assemblage of enargite, chalcocite, and digenite is indicative of magmatic fluids (Einaudi et al., 2003). The transition from low- to intermediate- and to high-sulfidation stages has been documented in other Cordilleran deposits of Central Peru, such as Morococha, Cerro de Pasco, and Ayawilca (Catchpole et al., 2015; Rottier et al., 2016; Fontboté, 2020;

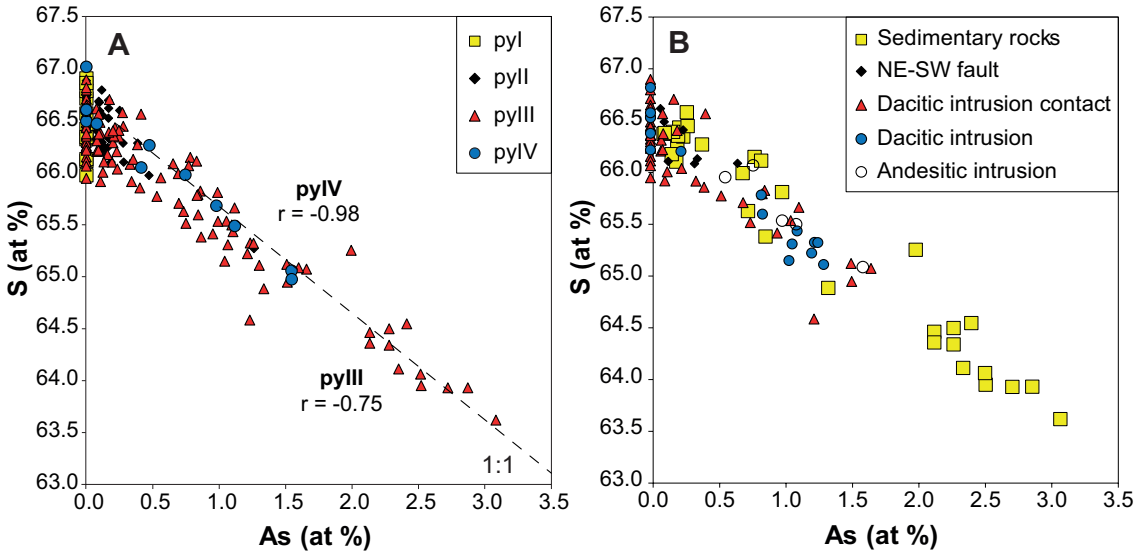

Fig. 9. Electron probe microanalyses (in at %) of pyrite from the Shahuindo deposit. A. As versus S for the indicated pyrite generations. Dashed lines represent 1:1 correlation; r is the Pearson correlation coefficient. B. As versus S for the pyIII generation from different host-rock types or tectonic position.

Benites et al., 2022). Indeed, the different sulfidation stages identified in our study are rather similar to stages A to C of most Cordilleran-type deposits that are generally explained by decreasing temperature (Fontboté, 2018, 2020). However, the fundamental reasons for this evolution of sulfidation state may be different at Shahuindo and reflect the particularities of interaction of magmatic fluids with C_{org}-rich rocks, as will be shown below. Due to high reactivity of sedimentary organic matter, initially acidic, oxidized magmatic-derived fluids may have completely lost their acidic and oxidizing properties by interacting with fresh portions of C_{org}-bearing rocks, resulting in the low-sulfidation mineral assemblages at early stages. Subsequent portions of fluids may have passed through progressively more and more altered rocks having less and less buffering capacity and resulted in an apparent increase in sulfidation state conditions from pyII to pyIV generations. This interpretation is consistent with the thermodynamic modeling that will be discussed further below.

Gold-arsenic relationships in pyrite

Gold and arsenic contents in diagenetic pyrite (pyI) from the Shahuindo deposit are similar to those observed in sedimentary pyrite from other provinces worldwide such as Sukhoi Log (Russia), Bendigo (Australia), and the Otago schist in New Zealand (Large et al., 2009, 2012). At Shahuindo, no clear correlation emerges between gold and arsenic at this early stage, suggesting that these elements were decoupled at the time of diagenesis, before ore formation. Hydrothermal pyII, pyIII, and pyIV display, in contrast, positive correlations between Au and As with the maximum of Au-As enrichment attained during pyIII deposition. The maximum As concentration value of 5.6 wt % in pyIII is consistent with theoretical predictions of As-S solid-solution range in pyrite, which may extend to ~6 wt % As incorporated in the pyrite structure, without formation of arsenopyrite domains (Reich and Becker, 2006). This As saturation limit in pyrite is also in agreement with the paragenetic sequence showing that arsenopyrite and pyIII were coeval. A maximum content of 460 ppm Au analyzed by LA-ICP-MS in arsenopyrite of the pyIII stage is consistent with both natural and experimental data, which indicate that arsenopyrite incorporates much higher Au contents than coexisting pyrite (up to 1–2 wt %; Boiron et al., 1989; Wu and Delbove, 1989; Fleet and Mumin, 1997; Pokrovski et al., 2021). The arsenic-gold coupling in hydrothermal pyrite evidenced in our study is consistent with the common As-Au associations and As control on Au incorporation in pyrite, initially identified in Carlin-type deposits (e.g., Radtke et al., 1972; Wells and Mullens, 1973; Fleet and Mumin, 1997; Simon et al., 1999; Cline, 2001; Cline et al., 2005; Muntean et al., 2011) and later recognized in many other gold deposit types such as orogenic (e.g., Cook and Chryssoulis, 1990; Large et al., 2007; Velasquez et al., 2014; Belousov et al., 2016), intrusion-related (e.g., Voute et al., 2019), porphyry Cu-Au (e.g., Deditius et al., 2014), and volcanogenic massive sulfide (e.g., Deditius et al., 2014; Belousov et al., 2016). More recently, the key role of arsenic in invisible gold incorporation into pyrite has been demonstrated by direct laboratory experiments coupled with in situ X-ray absorption spectroscopy (e.g., Kusebauch et al., 2019; Pokrovski et al., 2019, 2021). Our findings thus confirm the recent proposition, based on experimental and spectroscopic evidence, that incorporation of gold in pyrite and arsenopyrite from gold-undersaturated fluids during pyritization of the host rock occurs through a redox-driven reaction of Au binding to As in the structures of pyIII and apyIII (Pokrovski et al., 2021). In contrast, gold occurring in much lower concentrations in As-poor diagenetic pyrite (pyI) is decoupled from arsenic and is likely being chemisorbed on the pyrite surface and/or incorporated in structural defects in the form of Au sulfide complexes (e.g., Pokrovski et al., 2019). Gold concentrations increase in pyIII that is enriched in arsenic, which is also in line with the coexistence of Au-rich apyIII. The formation of both As-rich phases is likely favored by an increase in As

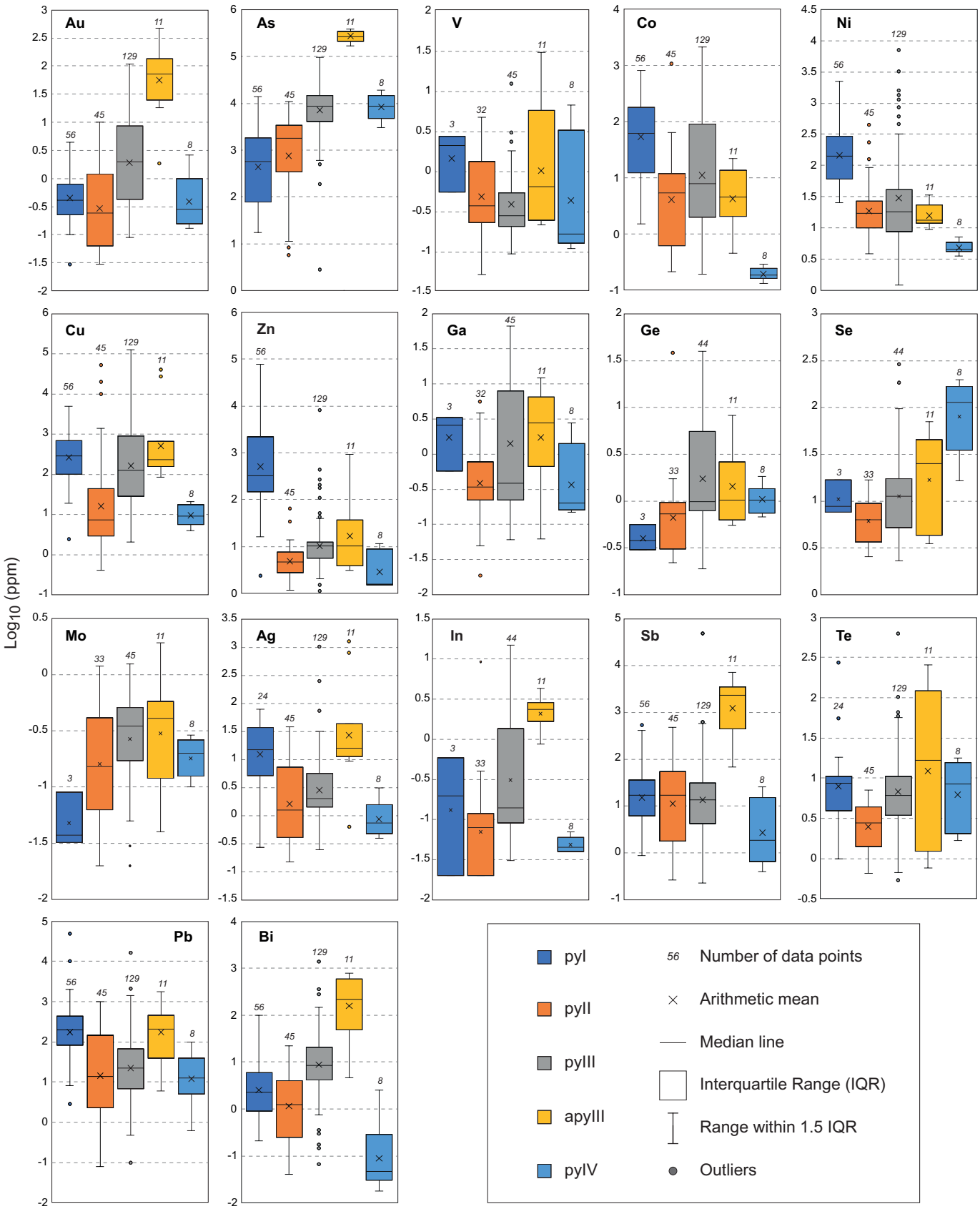

Fig. 10. Box plots showing the contents of 17 trace elements (in log_{10} units of ppm) analyzed by laser ablation-inductively coupled plasma-mass spectrometry in the four pyrite generations (pyI to pyIV) and in arsenopyrite (apyIII, belonging to pyIII generation).

Table 4. Summary of LA-ICP-MS Analyses (in ppm) of Selected Arsenopyrite and Pyrite Grains from the Shahuindo Mine

Mineral		V	Co	Ni	Cu	Zn	Ga	Ge	As	Se	Mo	Ag	In	Sb	Te	Au	Pb	Bi
pyI	Min	0.5	1.5	25	2.5	2.4	0.6	0.3	17	7.7	0.03	0.3	0.02	0.9	1.0	0.03	2.8	0.2
n = 56	Max	2.6	790	2,250	4,970	77,860	3.3	0.56	13,670	17	0.09	78	0.6	530	270	4.5	48,520	99
	Mean	1.4	53	145	264	499	1.7	0.40	43	10	0.05	12	0.11	15	7.8	0.3	177	2.5
pyII	Min	0.05	0.2	3.9	0.4	1.2	0.02	0.2	6	2.6	0.02	0.15	0.02	0.27	0.65	0.03	0.08	0.04
n = 45	Max	4.6	1,070	450	53,660	65	5.5	1.74	10,610	17	1.2	38	0.4	480	7.1	9.9	1,010	23
	Mean	0.5	4.0	19	16	4.9	0.4	0.5803	729	6.0	0.16	1.6	0.06	11	2.5	1.0	14	1.1
pyIII	Min	0.09	0.2	1.2	2.1	1.1	0.06	0.2	3	2.3	0.02	0.2	0.03	0.2	0.5	0.09	0.1	0.07
n = 129	Max	11.9	2,070	7,020	125,500	8,270	66.1	40	94,270	290	1.3	1,030	14.8	48,740	620	110	16,210	1,380
	Mean	0.4	11	30	166	10	1.4	1.9	6,950	11	0.27	2.9	0.3	14	6.8	7.0	23	8.9
apyIII	Min	0.2	0.5	9.5	84	3.1	0.06	0.6	163,150[1]	3.5	0.04	0.6	0.9	70	0.8	1.8	6.0	4.7
n = 11	Max	29	22	33.6	40,320	940	12.3	8.2	377,170[1]	70.8	1.9	1,260	4.3	7,280	250	460	1,780	790
	Mean	1.0	4.2	16	520	17	1.7	1.4	263,070[1]	17	0.3	27	2.1	1,249	12	55	171	158
pyIV	Min	0.1	0.1	3.6	4.0	1.5	0.2	0.7	2,970	17	0.1	0.4	0.04	0.4	1.7	0.1	0.6	0.02
n = 8	Max	6.4	0.3	7.2	21	12	2.8	1.8	18,870	200	0.3	3.2	0.07	26	18	2.6	100	2.6
	Mean	0.4	0.2	4.9	9.5	2.9	0.4	1.0	8,140	80	0.2	0.9	0.05	2.7	6.2	0.7	12	0.09

Abbreviations: n = number of LA spot analyses, LA-ICP-MS = laser ablation-inductively coupled plasma-mass spectrometry, Mean = arithmetic mean value
[1]Absolute values underestimated because of lack of external standard

concentration in the fluid together with an increase in pH, as may be inferred by the change from sericitic-type alteration (pyII stage, acidic pH) to carbonate mineral deposition (pyIII stage, near-neutral pH).

In summary, gold was likely deposited from a metal-undersaturated fluid and incorporated in a chemically bound state mainly into arsenian pyIII and arsenopyrite from reducing (H_2S-dominating) fluids of near-neutral pH—conditions that likely generated from the interaction of magmatic-derived fluid with organic-bearing sediments. At a somewhat later time, upon (partial) exhaustion of the organic sediment buffering capacities, conditions evolved to more oxidizing and acidic. Circulation of oxidizing (at the sulfate-sulfide coexistence boundary), acidic magmatic fluids with deposition of alunite and enargite indicate an environment typical of the upper part of a porphyry system (White and Hedenquist, 1990; Hedenquist and Lowenstern, 1994; Einaudi et al., 2003; Sillitoe and Hedenquist, 2003; Fontboté et al., 2017). The change from low- to intermediate- and to high-sulfidation states observed in most Peruvian Cordilleran-type deposits is commonly attributed to hydrolysis of SO_2 from magmatic acidic fluids progressively interacting with Paleozoic graphite-bearing phyllites, which have lesser abundance and weaker buffering capacities than C_{org} rocks at Shahuindo (Kouzmanov and Pokrovski, 2012; Fontboté, 2018, 2020; Benites et al., 2022). Further evidence for a magmatic origin of the gold-bearing fluid is provided by the presence of other trace elements such as Se, Ge, Mo, In, Ga, and Bi in pyIII. These elements are commonly found in pyrite formed in epithermal deposits hosted in volcanic rocks (Sykora et al., 2008; Ishida et al., 2022). This signature is in agreement with the elevated volatility and solubility of these elements in hydrothermal-magmatic fluids or vapor phases, produced during porphyry stages by magmatic fluid unmixing (e.g., Kouzmanov and Pokrovski, 2012; Pokrovski et al., 2013; Large et al., 2016).

Source of elements and mass balance considerations

Gold concentrations above 20 ppb were systematically analyzed in samples showing either direct (hydrothermal pyrite with or without other sulfides) or indirect (Fe excess compared to FeS_2 assuming all S in pyrite; Table 3) evidence of hydrothermal mineralization. In contrast, barren host-rock samples collected outside and within the deposit show gold content below 1 ppb. This value is lower than those suggested by Large et al. (2011) in a compilation of black shale compositions from Sukhoi Log, Carlin, and Bendigo. Our Au values in unmineralized samples also fall in the lower part of the concentration range of the typical black shales (0.2–11 ppb Au) of Johnson et al. (2017) and are far below the mean Au content of 7 ppb of carbonaceous black shales reported by Crocket (1991). The elevated Au values in sedimentary rocks cited in the previous work above might partly be due to higher detection limits of the analytical techniques used in those studies. Therefore, a value of 1 ppb Au can be used as a more realistic background value for the sediments of the Chicama Formation and the Goyllarisquizga Group that host part of the Shahuindo gold mineralization. The other part of gold at Shahuindo is hosted by strongly altered andesitic and dacitic intrusions. The gold content for andesitic to dacitic rocks is estimated to be 6 to 9 ppb (Moss et al., 2001; Chiaradia,

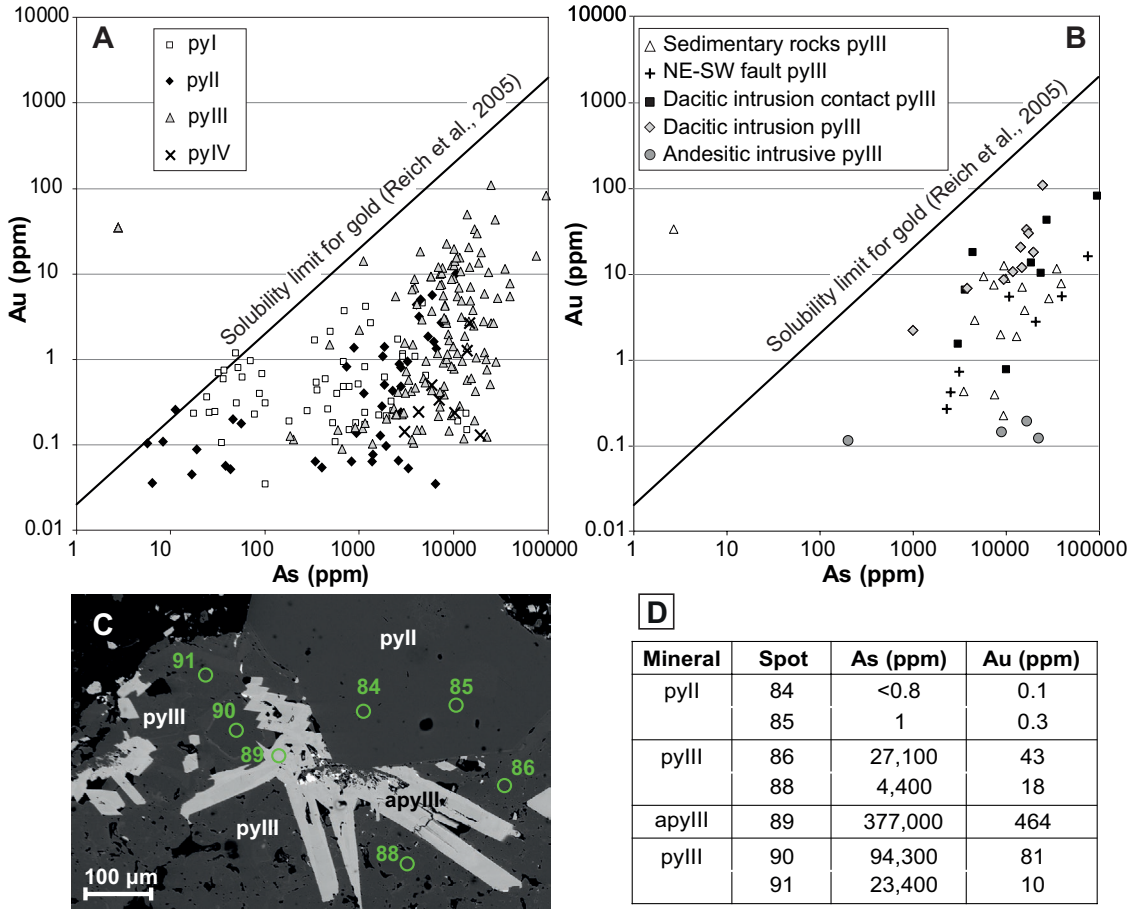

Mineral	Spot	As (ppm)	Au (ppm)
pyII	84	<0.8	0.1
	85	1	0.3
pyIII	86	27,100	43
	88	4,400	18
apyIII	89	377,000	464
pyIII	90	94,300	81
	91	23,400	10

Fig. 11. Results of laser ablation-inductively coupled plasma-mass spectrometry (LA-ICP-MS) analyses of gold and arsenic concentrations in representative pyrite (py I to pyIV) and arsenopyrite samples from the Shahuindo deposit. A. Logarithmic plot of As versus Au for all pyrite generations. B. Logarithmic plot of As versus Au for pyIII from different host rocks. C. Scanning electron microscope photomicrograph of an Au-poor pyII grain with later Au- and As-bearing pyIII and coexisting arsenopyrite (apyIII); green circles show the position of LA-ICP-MS laser spots. D. As and Au concentrations obtained in the laser ablation spots indicated in C.

2020). We therefore adopted a value of 4 ppb Au as the most plausible background level for the global source rock, composed of sediments crosscut by intrusions, and we used this value in the mass balance analysis that follows.

Reserves estimates at Shahuindo are 59 t Au in the oxidized currently exploited part of the deposit. Considering a similar amount of the underlying primary sulfide ore, a total endowment of 100 t Au would be a reasonable estimate. Assuming 4 ppb Au in the source rock (density of 2.6 g/cm^3), with 50% efficiency for gold mobilization from the rock and 50% efficiency for subsequent Au deposition, 38.4 km^3 (3.4 × 3.4 × 3.4 km) of source rock would be necessary to supply 100 t of gold. This estimated volume is conservative because of the presence of numerous impermeable shale horizons, particularly in the Santa and Carhuaz Formations, which show no evidence of hydrothermal alteration. This mass balance analysis indicates that the host sedimentary rock alone cannot be regarded as the only source for gold in the deposit. This is because the potential size of the Shahuindo hydrothermal system, as estimated by the exploration drilling program (Defilippi et al., 2016) (Fig. 3), is less than ~2 km (≤8 km^3), which is almost five times smaller than the necessary volume calculated above to account for the known Au tonnage. In addition, there is no evidence of massive release of gold from diagenetic pyrite related to a regional metamorphic event as in orogenic gold settings. The iron content of the host rock is also a key parameter, as its abundance and reactivity partly controls the H_2S fluid content and the resulting Au dissolved concentration in the form of sulfide complexes. The analyzed sedimentary rocks show an excess of iron compared to FeS_2, which decreases when approaching the mineralized zones. In the case of the intrusions, sericitic alteration is accompanied by iron sulfidation of mafic minerals. Iron sourced from magmatic minerals is sufficient to account for the abundance of pyrite in the system. However, an additional contribution of iron directly from magmatic fluids is also possible and would be in line with the large amount of pyrite observed within the massive contact bodies. Note that low-salinity aqueous fluids of magmatic origin, typical of porphyry-epithermal settings, are able to transport as much as tens of parts per million Au, 100 to 1,000 ppm As, and 10,000 ppm Fe, as demonstrated by the large body of direct fluid inclusion analyses available (e.g., Kouzmanov and Pokrovski, 2012). Our statistical sample is, however, not

sufficiently large to provide a more quantitative estimate of the amounts of the different pyrite types and their respective gold contributions compared to the whole mineralized rock. Nevertheless, our rough mass balance assessment above, combined with the observed mineral assemblages, and independent geochemical evidence from trace element patterns in pyrite, strongly suggests that a magmatic-hydrothermal source was the major metal supplier to the deposit for both Au and As and partly for Fe. In-depth understanding of the mechanisms of Au transport and precipitation and the effects of organic carbon and arsenic may be helped by physical-chemical modeling, as discussed below.

Thermodynamic modeling of mechanisms of gold and arsenic transport and precipitation

Based on the constraints detailed above, we simulated interactions of an Au-As-Fe–bearing hydrothermal fluid with an organic carbon-bearing rock, in an attempt to model gold transport and concentration mechanisms as they may have occurred in the Shahuindo deposit. In these simulations, gold and arsenic were assumed to be transported by moderate-salinity (7 wt % NaCl equiv; Na/K = 10) S-bearing (0.6 wt % total S) acidic fluids (pH < 3), such as typically exsolved in magmatic systems (Heinrich, 2005; Fontboté et al., 2017; references therein). We chose a wide range of redox potential (from strongly oxidized, sulfate-dominated, to strongly reduced, hydrogen sulfide-dominated), between 150° and 350°C at pressures of 100 to 1,000 bar. These conditions are consistent with the temperatures and sulfidation stages inferred in this study from mineral assemblages and with the general epithermal-like setting of the deposit (Defilippi et al., 2016). The fluid was assumed to interact with hydrocarbon-bearing sandstone/shale such as the host rocks of the sedimentary basin. In order to best evaluate the maximum potential for the fluid to transport Au and Fe, we assumed saturation with respect to metallic gold and pyrite. Arsenic was also added to the initial fluid at a level of 100 ppm, a typical concentration inferred from published fluid inclusion analyses from epithermal deposits (e.g., Kouzmanov and Pokrovski, 2012). Figure 12 shows the evolution of Au, Fe, and As, as well as sulfate, sulfide, trisulfur ion, methane, carbonate, and hydrogen concentrations, oxygen fugacity, and pH in two initially acidic (pH ~2.5) S-bearing (0.6 wt % total S) fluids of contrasting redox potential. One fluid is reduced (oxygen fugacity in $\log f_{O_2}$ relative to the conventional hematite-magnetite [HM] buffer, HM – 3) and the other is oxidized ($\log f_{O_2}$ = HM + 3). Each fluid type was allowed to interact at 300°C and 500 bar with a hydrocarbon-bearing rock (C_{org}, with a molal C/H ratio of 1) with progressively increasing modal C_{org} abundance (Fig. 12). Calculations at other T-P values within the chosen epithermal range (150°–350°C, 100–1,000 bar), and for rocks with different types of organic matter ranging from oil-like compositions (C/H ratio ~½) to matured kerogen (C/H ratio ~2) and to graphite (C/H ratio ∞), yielded very similar solubility trends and thus are not reported here in detail.

Our results show that the effect of organic matter on Au, As, and Fe solubility is strongly conditioned by the initial redox state of the fluid, yielding highly contrasting solubility trends for the three metals. These trends are driven by changes in three key parameters—redox potential, pH, and sulfide activity—as they affect the solubility reactions for native gold and pyrite as well as the degree of arsenic and gold incorporation in pyrite:

$$Au\ (metal) + \tfrac{1}{4}O_2 + H_2S_{(aq)} = AuHS^0_{(aq)} + \tfrac{1}{2}H_2O \quad (1a)$$

$$Au\ (metal) + \tfrac{1}{4}O_2 + 2H_2S_{(aq)} = Au(HS)^-_2 + H^+ + \tfrac{1}{2}H_2O \quad (1b)$$

$$FeS_2\ (pyrite) + 2H^+ + 2Cl^- + H_2O = FeCl^0_{2(aq)} + 2H_2S_{(aq)} + \tfrac{1}{2}O_2 \quad (2)$$

$$FeS_2\ (pyrite) + As(OH)^0_{3(aq)} = [FeAsS] + H_2S(aq) + 1\tfrac{1}{4}O_2 + \tfrac{1}{2}H_2O, \quad (3)$$

where [FeAsS] denotes arsenopyrite or arsenian pyrite solid solution for simplicity. All reaction constituents other than pyrite, arsenopyrite, and gold metal are aqueous species in the single-phase liquid-like fluid. In these reactions, we have chosen O_2 because oxygen fugacity is the most widely admitted redox parameter and is conveniently referenced to common mineral buffers typical of hydrothermal systems (e.g., HM, or pyrite-pyrrhotite-magnetite [PPM]). Note that equivalent reactions may be written with any other oxidizing or reducing component, such as H_2, CH_4, CO_2, or CO, with no effect on the thermodynamic equilibrium relationships.

Figure 12 shows that the changes in f_{O_2}, pH, and sulfide activity are rather minor for an initial strongly reduced H_2S-dominated fluid interacting with organic carbon. This is because both fluid and rock have similar redox potential. In addition, the dissolution of hydrocarbon in water, leading to the formation of uncharged dominant species, CO_2, CH_4, and graphite, cannot generate significant changes in fluid acidity (Fig. 12A, B). As a result, the solubility of Fe increases only slightly and that of Au and As decreases slightly when the fluid reacts with the first portions of sedimentary rock. Such H_2S-rich acidic fluid can thus transport significant concentrations of Fe (~1,000 ppm) but rather low concentrations of Au (0.1 ppm) and As (<10 ppm), the latter being preferentially incorporated in arsenian pyrite (up to 10,000 ppm in the mineral). Thus, such fluids cannot transport significant amounts of As and Au together. Furthermore, they would rapidly lose their contents in the presence of reactive ferrous iron (FeO) present in carbonates and mafic silicates. These reactions altogether would lead to both a decrease in pH and consumption of H_2S through precipitation of pyrite (inverse of reaction 2), and concomitant gold deposition, mostly via decrease in H_2S activity in the fluid (inverse of reaction 1a, b).

A different scenario occurs for a more oxidized fluid containing sulfate upon interaction with the carbonaceous rock (Fig. 12C, D). Such a fluid, which initially transports Fe, As, and Au with concentrations of up to 1,000, 100, and 1 ppm, respectively, similar to the reduced fluid above, exhibits drastic changes when interacting with organic carbon. It can be seen in Figure 12C that Fe concentrations drop as much as six orders of magnitude even in the presence of quite low contents of C_{org} in the rock (<2 mol %), whereas As concentrations remain constant in the fluid, and only a small As fraction is incorporated into pyrite at tenors of few parts per million As. It is only when the aqueous sulfate is mostly consumed by reduction by organic carbon (C_{org} in rock >3 mol %) that As is incorporated into pyrite in amounts comparable to the naturally observed levels as found in this study (>10–100 ppm

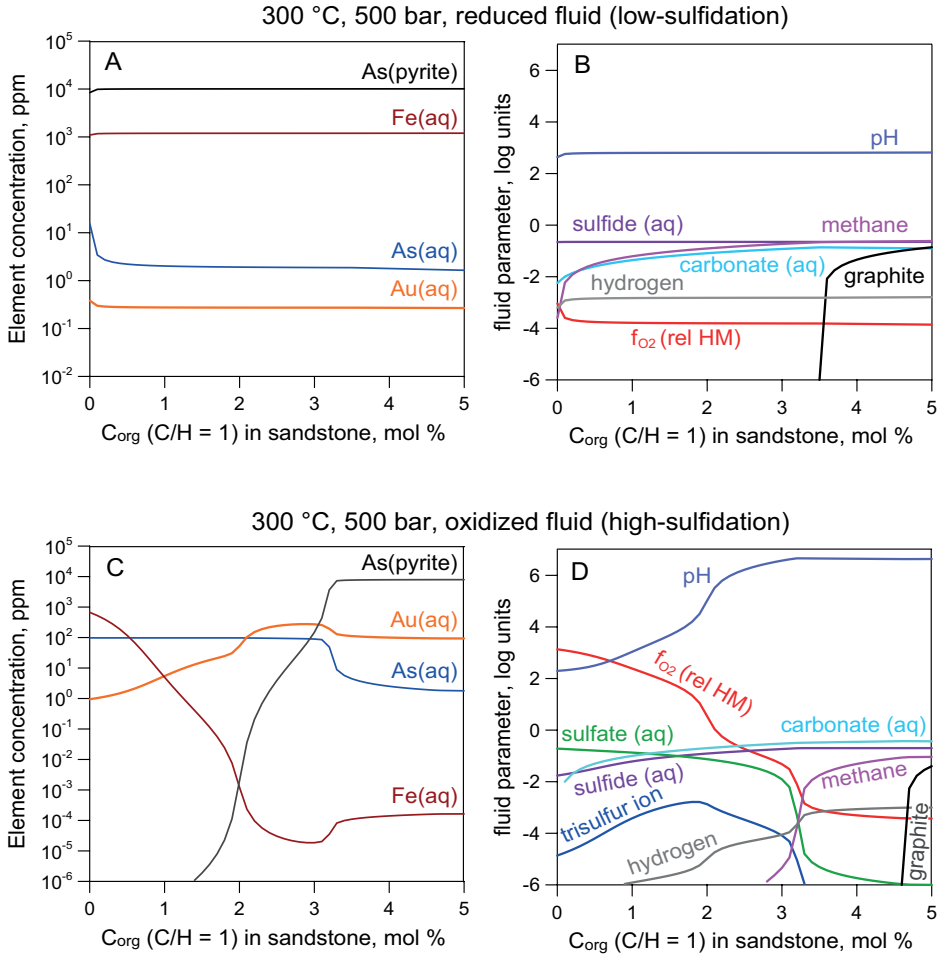

Fig. 12. Diagrams showing the results of thermodynamic modeling of fluid-rock interactions in the context of the Shahuindo deposit. Two contrasting cases of the initial S-Au-As-Fe–bearing epithermal fluid are monitored: (A, B) reduced (H_2S-dominated) and (C, D) oxidized (sulfate-dominated). The low-salinity acidic (7 wt % NaCl equiv; 1 m NaCl + 0.1 m KCl + 0.05 HCl, pH = 2.5) magmatic-derived fluid containing 100 ppm As and saturated with pyrite and metallic gold was allowed to react at 300°C and 500 bar with a hydrocarbon-bearing shale at a mass fluid/rock ratio of 1:1 as a function of organic carbon content in the rock (C_{org}, with C/H atomic ratio of 1). A and C. Concentrations of dissolved Au, Fe, and As in the fluid (aq) and of As in pyrite as a function of CH content for a reduced (f_{O_2} is close to the conventional pyrite-pyrrhotite-magnetite redox buffer, PPM ≈ HM – 3) and an oxidized (f_{O_2} is above that of the hematite-magnetite buffer, HM + 3) initial fluid. B and D. Corresponding evolution of the fluid-phase concentrations (in log10 units of molality) of sulfide, sulfate, the S^{3-} ion, dissolved hydrogen, and carbon-bearing species, pH, and oxygen fugacity (relative to the HM buffer). It can be seen that organic carbon may exert a contrasting effect on the transport of different metals, depending on the initial fluid properties and the organic carbon (C_{org}) content. In particular, organic matter may promote, rather than limit, gold fluid transport in C_{org}-bearing sedimentary/metamorphic rocks (see text for discussion).

As in pyIII and apyIII). Gold shows a spectacular increase in its solubility, attaining several hundreds of parts per million Au at C contents in the system comparable to that of S (at C_{org} >2–3 mol %), followed by a slight decrease (to 10s ppm Au) when approaching the graphite saturation. These contrasting changes are fundamentally driven by the evolution of pH and redox of the sulfate-bearing fluid, which are controlled by thermochemical sulfate reduction (TSR) reactions:

$$SO_4^{2-} + CH_4 + 2\,H^+ = H_2S_{(aq)} + CO_2 + 2H_2O \quad (4)$$

$$CH_4 + 2O_2 = CO_2 + 2H_2O. \quad (5)$$

It can be seen in Figure 12D that proton-consuming reaction (4) induces a pH increase of >4 units (from ~2 to >6) upon fluid infiltration into the carbonaceous rock. At the same time, reaction (5), which consumes oxygen, leads to an f_{O_2} decrease of five to six orders of magnitude. Note that reaction (1b) imposes Au solubility to be linearly proportional to the H^+ activity, i.e., inverse of pH, but to be proportional only to the power of one-fourth of f_{O_2}. Likewise, pyrite solubility (reaction 3) is proportional to the square-power of H^+, but to only the power of one-half of f_{O_2}. Although changes in H_2S upon fluid interaction with organic matter are relatively small compared to those in pH (1 log unit H_2S concentration vs. >4 log units in pH; Fig. 12D), they do contribute to favoring Au solubility, in particular for reaction (1b). Therefore, increase in pH (and partly in H_2S) upon sulfate reduction by organic carbon appears to exert the major control on Au solubility for a typical epithermal fluid in a high-sulfidation regime. Thus, independently of the exact scenario of Fe and Au fluid-phase transport, whose details would depend on a fine interplay

between the exact fluid initial redox, S and C_{org} contents of the system, and the fluid/rock ratio, the effect of pH increase on Au solubility is generally much greater than the opposite effect of f_{O_2} decrease. Thus, our modeling quantitatively demonstrates that TSR reactions of epithermal fluids may strongly enhance gold mobility and focused transfer from a magmatic source to a sedimentary organic-bearing rock sequence and its subsequent deposition in favorable structures such as anticlines. Hence, our findings question common belief that organic matter would be unfavorable for gold transport and therefore act as trap for this metal in hydrothermal systems (Radtke and Scheiner, 1970; Bierlein et al., 2001; Zhou et al., 2010; Phillips and Powell, 2013).

Gold incorporation in arsenian pyrite and arsenopyrite

Our quantitative thermodynamic modeling demonstrates that parts per million-level Au concentrations can be transported by moderately reduced to moderately oxidized (sulfate-sulfide coexistence) S-bearing epithermal fluids through organic-rich sedimentary rocks, without reaching saturation with the metal. Such gold metal-undersaturated fluids may lose their dissolved gold content by Au incorporation to arsenian pyrite in a chemically bound state. Although quantitative thermodynamic models of chemically bound Au incorporation in arsenian pyrite are not available at present, direct X-ray absorption spectroscopy data show Au to substitute for Fe in the octahedral sites by forming As-rich [$Au(As,S)_6$] arsenopyrite-like moieties (Pokrovski et al., 2021). Combining this speciation data with a recent thermodynamic model proposed for arsenopyrite (Pokrovski et al., 2021), the following formal reaction may be considered for Au incorporation in arsenian pyrite:

$$Au(HS)_2^- + H^+ + As(OH)_{3(aq)}^0 = [AuAsS]_{pyrite} + \tfrac{1}{2}O_2 + H_2S_{(aq)} + 2H_2O, \quad (6)$$

where $[AuAsS]_{pyrite}$ is the mole fraction of the fictive Au end member in the arsenian pyrite solid solution, and $Au(HS)_2^-$ and $As(OH)_3$ are the activities of the major Au and As aqueous species in the fluid. It can be seen from reaction (6) that the incorporation of Au in pyrite is directly favored by (1) higher Au and As dissolved concentrations, (2) more reducing conditions, (3) lower H_2S contents in the fluid, and (4) near-neutral pH at which Au is the most soluble as dihydrosulfide complexes. These trends are in good qualitative agreement with the increase of invisible Au concentrations in pyrite from the As-poor pyII of the low-sulfidation stage to As-rich pyIII (intermediate-sulfidation) and subsequent decrease in the more oxidized pyIV generation (high-sulfidation stage). More quantitative analysis of reaction (6) would require numerical values of its thermodynamic constant at a given T-P, coupled with more direct knowledge of the fluid composition gained from fluid inclusions, which are not presently available at Shahuindo. In the meantime, recent pyrite-fluid gold partitioning coefficients, experimentally measured by Kusebauch et al. (2019) at 200°C and Pokrovski et al. (2019, 2021) at 300° to 450°C, may be used for first-order estimations. Using an Au partition coefficient range of 100 to 1,000 between an arsenian pyrite with 0.1 to 1.0 wt % As and an S-bearing fluid carrying 0.1 to 1 ppm of Au (i.e., the typical Au concentration in epithermal porphyry-related fluids; Kouzmanov and Pokrovski, 2012), it can be estimated that such a pyrite would incorporate 10 to 1,000 ppm of Au in a bound state. Remarkably, such predicted tenors are of the same order of magnitude as those measured in arsenian pyrites and arsenopyrites of this and many previous studies (Cathelineau et al., 1989; Cook and Chryssoulis, 1990; Fleet and Mumin, 1997; Simon et al., 1999; Reich et al., 2005; Muntean et al., 2011; Deditius et al., 2014; Belousov et al., 2016; Voute et al., 2019). As a conclusion, our thermodynamic analysis attests for the large potential capacity of As- and S-bearing fluids for focused Au transfer from magmatic settings and subsequent Au intake in arsenian pyrite in structural traps in organic carbon-bearing sedimentary basins.

Formation model for the Shahuindo deposit

The structural analysis, coupled with geochronological data, paragenetic sequence, mineralization and host-rock geochemistry, and thermodynamic modeling presented here, allows us to propose a new model for the Au-bearing magmatic-hydrothermal fluid evolution in the sedimentary setting of the Shahuindo deposit (Fig. 13). A magmatic source for Au, As, and partly Fe is supported by the solubility of these elements in fluids typical of the epithermal conditions that prevailed in the system (Fig. 12) as well as by mass balance constraints attesting that the amount of gold initially present in the sedimentary host rocks is insufficient to account for the total tonnage of the deposit. Dacitic intrusions rooted in a laccolith at depth were emplaced along thrust faults, anticline axial planes, and northeast-southwest transverse faults of the Algamarca-Shahuindo imbricate system. Gold- and arsenic-bearing aqueous fluids (possibly of variable sulfidation state) exsolved at depth from the crystallizing igneous complex and ascended into the sedimentary basin along the same paths as the intrusions. During the fluid ascent, its interactions with the sedimentary formations rich in organic carbon allowed for efficient and focused dissolved gold transport, without reaching saturation with metallic gold. This gold transfer occurred through the sedimentary sequence to structural (e.g., fractured anticline hinges, brecciated intrusion-sediment contact) or lithological (e.g., layers of permeable rock between less permeable strata) traps that resemble those commonly observed in oil systems. Entrapment of the Au-As-H_2S(-Fe)–bearing fluid in zones of reduced permeability, followed by its eventual cooling, favored invisible chemically bound gold incorporation in arsenian pyrite, thereby resulting in the formation of the orebodies.

The enhancement of hydrothermal gold transport by pH neutralization produced by feldspar alteration in igneous rocks or by calcite dissolution in sediments has been predicted thermodynamically in the literature to account for the large gold mobility in epithermal settings hosted within organic carbon-poor altered volcanic rocks (Heinrich, 2005). The chemical-level control of the enhancement of gold solubility is fundamentally similar in our model, as driven by reaction (1b), which is favored by both increasing pH and H_2S content. However, in our case the cause of this enhancement is the interaction of the fluid with carbonaceous matter, followed by subsequent gold incorporation in arsenian pyrite. Such a new combined mechanism of gold transport and precipitation in a sedimentary setting has not yet been documented.

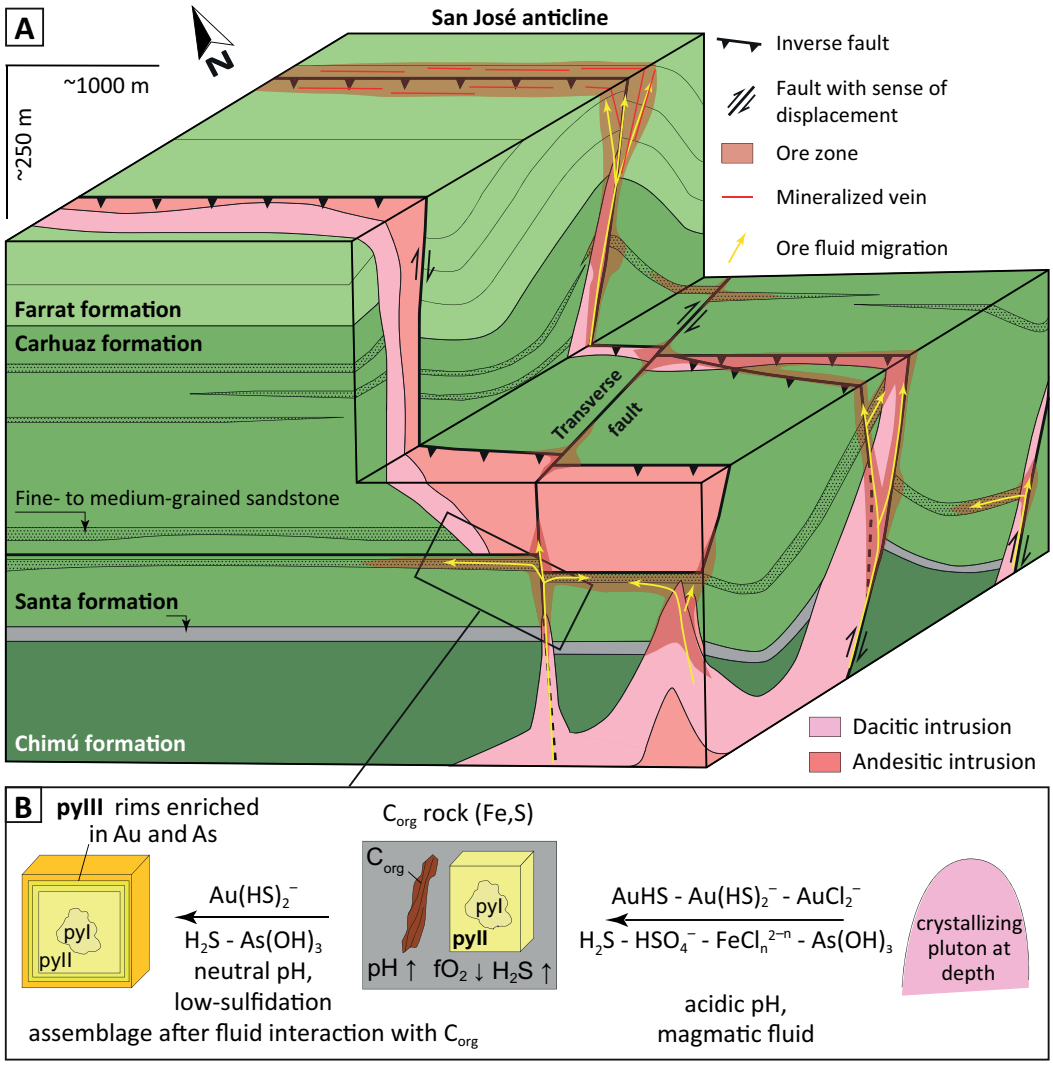

Fig. 13. A. Block diagram model of the Shahuindo deposit showing the location of the San José anticline, thrust and transverse faults, intrusion contacts, and permeable fine- to medium-grained sandstone horizons that control the location of gold ore. B. Schematic representation of the mineralization process, with gold transport by a magmatic fluid during its interaction with organic carbon (C_{org})-bearing sedimentary rocks, and subsequent gold scavenging from the fluid by arsenian pyrite. The key aqueous species of gold and associated elements are indicated.

This scenario is also different from the one generally assumed for Carlin-type deposits, where Au-bearing arsenian pyrite is formed by direct sulfidation of Fe-bearing carbonate rocks (Cline et al., 2005; Muntean et al., 2011; Kusebauch et al., 2019). Our mechanism is also different from those invoked in many other types of epithermal gold deposits, where boiling and fluid mixing in rock types lacking organic carbon are considered to be the dominant processes for gold deposition (e.g., Simmons et al., 2005, 2020). Although invisible gold in arsenian pyrite has been also recognized in different types of ore deposits such as orogenic (e.g., Large et al., 2007; Velasquez et al., 2014; Belousov et al., 2016; Simmons et al., 2020), intrusion-related (e.g., Voute et al., 2019), some porphyry Cu-Au (e.g., Deditius et al., 2014), and volcanogenic massive sulfide (e.g., Deditius et al., 2014; Belousov et al., 2016), its fraction appears to be small compared to the predominant visible metallic gold in those settings. In addition, the molecular state of invisible gold in pyrite from those settings (nanoparticulate metal vs. chemically bound) is not well established. In contrast, chemically bound gold incorporation in arsenian pyrite is clearly the main gold depositional process at Shahuindo and suggests a new, previously disregarded mechanism for gold transport and deposition in organic carbon-rich sedimentary rocks in an epithermal setting.

Comparison with other gold deposits

The Shahuindo deposit shares some common features with Carlin-type deposits (Hofstra and Cline, 2000; Cline et al., 2005; Muntean et al., 2011; Rhys et al., 2015; Muntean and Cline, 2018; Henry et al., 2023), including (1) significant stratigraphic and structural ore control, (2) rarity of veins, (3) gold in a chemically bound state in arsenian pyrite, and (4) similar temperature and pressure conditions (150°–300°C, 100–1,000 bar). Conversely, Shahuindo differs from Carlin-type deposits by the following features: (1) apparently lower tonnages and grades (however, exploration in this area of the

Marañon fold-and-thrust belt is far more immature compared to the area of the Carlin trend), (2) a clearer genetic association between mineralization and coeval felsic magmatism as source of fluids and metals, (3) an episode of polymetallic mineralization, (4) high-sulfidation conditions reached locally, and (5) rarity of carbonates and lack of evidence of their sulfidation.

Shahuindo also displays some structural similarities with orogenic gold deposits hosted in carbonaceous sedimentary sequences. However, these deposits are believed to be formed through release of gold from diagenetic pyrite during regional metamorphism and associated compression. Gold deposition in such deposits occurred in anticlinal and/or thrust structures in higher and less metamorphosed portions of the sequence in response to sulfidation of the wall rock under relatively reducing conditions corresponding to the PPM mineral buffer (Mikucki, 1998; Goldfarb et al., 2005; Pitcairn et al., 2006; Large et al., 2011; Gaboury, 2013; Tomkins, 2013; Pokrovski et al., 2015). At Shahuindo, no evidence of regional metamorphism has been identified. Furthermore, the changing sulfidation conditions and the resulting hydrothermal alteration types are not compatible with a metamorphic model.

At Shahuindo, the presence of a significant magmatic-hydrothermal component of the fluids, the spatial association with intrusions, and the polymetallic stage are features in common with the distal disseminated gold ± silver deposit type (Cox, 1992; Muntean and Cline, 2018). In contrast, an important difference is the absence of a proximal zone that is typical in porphyry/skarn mineralization. Other notable differences from these distal deposits are the abundance of invisible gold mineralization and a large range of sulfidation conditions.

Gold association with low-sulfidation mineral assemblages at Shahuindo makes it similar to the low-sulfidation type of epithermal deposits. In addition, some low-sulfidation epithermal deposits contain auriferous pyrite, even though the gold speciation is not clear (John et al., 2003; Morishita et al., 2018). In contrast, in most classic low-sulfidation epithermal deposits, gold-bearing pyrite represents only a small fraction of the mineralization, in which gold occurs mainly as electrum (Au-Ag alloy). Furthermore, metal deposition in such deposits is usually accompanied by precipitation of large amounts of silica, carbonate, and adularia with textures indicative of boiling. Such features are not observed at Shahuindo.

The transition from low- to intermediate- and to high-sulfidation stages detected at Shahuindo may reflect the continued interaction of the magmatic fluids with the reactive C_{org}-bearing sedimentary rocks, with later fluid portions passing through already altered rocks, partly losing their chemical reactivity and buffering capacity. Alternatively, or in parallel, the evolution of the magmatic fluid itself from low-sulfidation to high-sulfidation might have contributed to this sequence. The latter is also a typical feature of many porphyry-related Zn-Pb-(Ag) deposits of central Peru known as Cordilleran-type deposits formed in an epithermal environment (Catchpole et al., 2015; Rottier et al., 2016; Fontboté, 2020; Benites et al., 2022). These deposits are believed to be formed via cooling of a metal-bearing fluid of magmatic origin in contact with silica-alumina-carbonate–bearing rocks. The Cordilleran-type deposits are, however, typically polymetallic (Cu, Zn, Pb, Ag) and relatively poor in gold. Thus, the Shahuindo deposit may represent a gold-rich end member where a previously disregarded very efficient mechanism of gold transport, concentration, and deposition in carbon-rich sedimentary setting played the major role.

Concluding Remarks

At Shahuindo, gold was transported and deposited after andesitic and dacitic bodies intruded into the sedimentary rocks. The shape of these bodies was controlled by thrusts that were imbricated in a northwest-southeast direction, along with associated folds and transverse faults that ran in a northeast-southwest direction. The auriferous orebodies were emplaced under similar structural control as the igneous bodies, with a strong influence from the anticlines, intrusion contacts, and permeable layers situated between impermeable horizons. This is a typical pattern seen in the formation of petroleum systems.

A thorough mineralogical and geochemical examination of the primary sulfide ore at Shahuindo has revealed that the majority of the gold is present in a chemically bound form in arsenian pyrite and arsenopyrite. These minerals were primarily deposited in a sedimentary environment under relatively low sulfidation conditions.

Additional geochemical analyses of the surrounding rock formations, coupled with mass balance constraints, have indicated that the sedimentary rocks alone did not contain sufficient gold, arsenic, and sulfur to be considered as the main source of the metals and ligands. Our results collectively support an igneous source of these metals, which may have been introduced via magmatic fluids exsolved from a plutonic complex crystallizing at depth.

The formation of the primary orebody could be envisaged by the following sequence of events. The ascent of magmatic aqueous fluids, likely acidic and rich in Au-As(-Fe) sulfate-sulfide, led to their interaction with the organic matter in the sedimentary sequence through TSR reactions. This process facilitated (or at least maintained) efficient transport of dissolved gold, enabling its deposition in structural and lithological traps in a chemically bound state within coprecipitating arsenian pyrite.

Implications for Exploration

These findings have significant implications for exploration, as invisible gold may be the main potential source of gold production in many countries (Berger et al., 2014; Volkov and Sidorov, 2017; Velasquez et al., 2020) despite the common a priori exclusion of refractory gold ores due to extraction difficulties. At the deposit scale, dating igneous intrusions, identifying arsenic, carbon, and gold geochemical anomalies in the rock and soil, and obtaining detailed trace element signatures in sulfide ore are of primary importance. At the regional scale, imbricated thrusts and folds should be targeted because they can provide pathways for magma and fluid migration to entrapment sites. Intersection of these structures with transverse faults may provide the necessary structural connectivity for an efficient flow of metal-bearing fluids sourced from crystalizing plutonic complexes at depth. This connectivity also makes it more probable for gold deposition to focus at such locations, which should be targeted during exploration. In

addition, anticlines, such as those in the thick, brittle Chimú and Farrat sandstones, are preferential zones for fluid entrapment between more impermeable rock types. Theses structural factors highlight the interest for constructing balanced cross sections in mineral exploration analogous to those extensively used by the oil industry for petroleum exploration in fold-and-thrust belts. These analogies with petroleum systems should prove helpful for developing mineral exploration strategies in sedimentary basins. Overall, our integrated structural, mineralogical, geochemical, and modeling study highlights an important potential of sedimentary carbon-bearing rocks in the formation and distribution of gold and associated critical metal resources.

Acknowledgments

This work was funded by the Consejo Nacional de Ciencia, Tecnología e Innovación Tecnológica-Fondo Nacional de Desarrollo Científico, Tecnológico y de Innovación Tecnológica (CONCYTEC-FONDECYT; project 425-2019) and the Institut Carnot ISIFoR (grants OrPet and AsCOCrit). We acknowledge support from the French-Peruvian cooperation program Evaluation-orientation de la Coopération Scientifique (ECOS)-Nord (grants ECOS P21U01 and 020-2021-FONDECYT). Petroleum Experts is acknowledged for providing the academic license of the MOVE software for structural interpretation. We thank A. Marquet, S. Gouy, and P. de Parseval for help with LA-ICP-MS and EPMA analyses, and C. Alvarez, R. Alva, and R. Vilchez of the Pan American Silver Corporation for their assistance in the field. Constructive comments by S. Simmons and S. Barker greatly improved the article.

REFERENCES

Akinfiev, N.N., and Diamond, L.W., 2003, Thermodynamic description of aqueous nonelectrolytes at infinite dilution over a wide range of state parameters: Geochimica et Cosmochimica Acta, v. 67, p. 613–627.

Arehart, G.B., Chryssoulis, S.L., and Kesler, S.E., 1993, Gold and arsenic in iron sulfides from sediment-hosted disseminated gold deposits: Implications for depositional processes: Economic Geology, v. 88, p. 171–185.

Bellier, O., Sébrier, M., Gasse, F., Fourtanier, E., and Robles, I., 1989, Evolution géodynamique mio-pliocène et quaternaire des bassins de la cordillère occidentale du Nord-Pérou: Les bassins de Cajabamba, San Marcos et Namora (département de Cajamarca): Géodynamique, v. 4, p. 93–118.

Belousov, I., Large, R.R., Meffre, S., Danyushevsky, L.V., Steadman, J., and Beardsmore, T., 2016, Pyrite compositions from VHMS and orogenic Au deposits in the Yilgarn craton, Western Australia: Implications for gold and copper exploration: Ore Geology Reviews, v. 79, p. 474–499.

Benavides-Cáceres, V., 1999, Orogenic evolution of the Peruvian Andes: The Andean cycle: Society of Economic Geologists, Special Publication 7, p. 61–107.

Benites, D., Torró, L., Vallance, J., Laurent, O., Quispe, P., Rosas, S., Uzieda, M.F., Holm-Denoma, C.S., Pianowski, L.S., Camprubí, A., et al., 2022, Geology, mineralogy, and cassiterite geochronology of the Ayawilca Zn-Pb-Ag-In-Sn-Cu deposit, Pasco, Peru: Mineralium Deposita, v. 57, p. 481–507.

Berger, V.I., Mosier, D.L., Bliss, J.D., and Moring, B.C., 2014, Sediment-hosted gold deposits of the world—database and grade and tonnage models: U.S. Geological Survey, Open-File Report 2014-1074, 51 p.

Bierlein, F.P., Cartwright, I., and McKnight, S., 2001, The role of carbonaceous "indicator" slates in the genesis of lode gold mineralization in the western Lachlan orogen, Victoria, southeastern Australia: Economic Geology, v. 96, p. 431–451.

Bissig, T., Ullrich, T., Tosdal, R., Friedman, R., and Ebert, S., 2008, The time-space distribution of Eocene to Miocene magmatism in the central Peruvian polymetallic province and its metallogenic implications: Journal of South American Earth Sciences, v. 26, p. 16–35.

Boiron, M.C., Cathelineau, M., and Trescases, J.J., 1989, Conditions of gold-bearing arsenopyrite crystallization in the Villeranges basin, Marche-Combrailles shear zone, France: A mineralogical and fluid inclusion study: Economic Geology, v. 84, p. 1340–1362.

Boyer, S.E., and Elliott, D., 1982, The geometry of thrust systems: American Association of Petroleum Geologists, AAPG Bulletin, v. 66, p. 1196–1230.

Calderon, Y., Baby, P., Vela, C., Hurtado, A., Eude, A., Roddaz, M., Brusset, S., Calvés, G., and Bolaños, R., 2017, Petroleum systems restoration of the Huallaga-Marañon Andean retroforeland basin, Peru: Petroleum systems analysis-case studies: American Association of Petroleum Geologists (AAPG), Memoir 114, p. 95–116.

Catchpole, H., Kouzmanov, K., Putlitz, B., Seo, J.H., and Fontboté, L., 2015, Zoned base metal mineralization in a porphyry system: Origin and evolution of mineralizing fluids in the Morococha district, Peru: Economic Geology, v. 110, p. 39–71.

Cathelineau, M., Boiron, M.C., Holliger, P., Marion, P., and Denis, M., 1989, Gold-rich arsenopyrites: Crystal-chemistry, gold location and state, physical and chemical conditions of crystallization: Economic Geology Monograph 6, p. 328–341.

Chase, M.W., Jr., 1998, NIST-JANAF thermochemical tables, 4th ed.: The Journal of Physical Chemistry, Monograph 9, http://webbook.nist.gov/chemistry.

Chew, D., Schaltegger, U., Košler, J., Whitehouse, M.J., Gutjahr, M., Spikings, R.A., and Mišković, A., 2007, U-Pb geochronologic evidence for the evolution of the Gondwanan margin of the north central Andes: Geological Society of America Bulletin, v. 119, p. 697–711.

Chiaradia, M., 2020, Gold endowments of porphyry deposits controlled by precipitation efficiency: Nature Communications, v. 11, p. 1–10.

Cline, J.S., 2001, Timing of gold and arsenic sulfide mineral deposition at the Getchell Carlin-type gold deposit, north-central Nevada: Economic Geology, v. 96, p. 75–89.

Cline, J.S., Hofstra, A.H., Muntean, J.L., Tosdal, R.M., and Hickey, K.A., 2005, Carlin-type gold deposits in Nevada: Critical geological characteristics and geologic models: Economic Geology 100th Anniversary Volume, p. 451–484.

Cook, N.J., and Chryssoulis, S.L., 1990, Concentrations of "invisible gold" in the common sulfides: The Canadian Mineralogist, v. 28, p. 1–16.

Cox, D.P., 1992, Descriptive model of distal disseminated Ag-Au deposits: U.S. Geological Survey, Bulletin 2004, p. 19–22.

Crocket, J.H., 1991, Distribution of gold in the Earth's crust, *in* Foster, R.P., ed., Gold metallogeny and exploration: London, New York, Chapman and Hall, p. 1–36.

Dahlstrom, C.D.A., 1969, Balanced cross-sections: Canadian Journal of Earth Sciences, v. 6, p. 743–757.

Deditius, A.P., Utsunomiya, S., Renock, D., Ewing, R.C., Ramana, C.V., Becker, U., and Kesler, S.E., 2008, A proposed new type of arsenian pyrite: Composition, nanostructure and geological significance: Geochimica et Cosmochimica Acta, v. 72, p. 2919–2933.

Deditius, A.P., Reich, M., Kesler, S.E., Utsunomiya, S., Chryssoulis, S.L., Walshe, J., and Ewing, R.C., 2014, The coupled geochemistry of Au and As in pyrite from hydrothermal ore deposits: Geochimica et Cosmochimica Acta, v. 140, p. 644–670.

Defilippi, C.E., Dyer, T., and Tietz, P., 2012, Technical report on the Shahuindo heap leach project Cajabamba, Peru: Sulliden Gold Corporation, Ltd, NI 43-101 Technical Report 420 p.

Defilippi, C.E., Muerhoff, C.V., and Williams, T., 2016, Technical report on the Shahuindo mine, Cajabamba, Peru: Tahoe Resources, NI 43-101 Technical Report, 307 p.

Disnar, J.R., and Sureau, J.F., 1990, Organic matter in ore genesis: Progress and perspectives: Organic Geochemistry, v. 16, p. 577–599.

Drennan, G.R., and Robb, L.J., 2006, The nature of hydrocarbons and related fluids in the Witwatersrand basin, South Africa: Their role in metal redistribution: Geological Society of America, Special Paper 405, p. 353–385.

Drennan, G.R., Boiron, M.C., Cathelineau, M., and Robb, L.J., 1999, Characteristics of post-depositional fluids in the Witwatersrand basin: Mineralogy and Petrology, v. 66, p. 83–109.

Einaudi, M.T., Hedenquist, J.W., and Inan, E.E., 2003, Sulfidation state of fluids in active and extinct hydrothermal systems: Transitions from porphyry to epithermal environments: Society of Economic Geologists, Special Publication 10, p. 285–313.

Elliott, D., 1983, The construction of balanced cross-sections: Journal of Structural Geology, v. 5, p. 101.

Eude, A., 2014, La croissance des Andes centrales du nord du Pérou (5-9°S): Propagation d'un prisme orogénique dans un contexte d'héritage tectonique

et de subduction plane: Unpublished Ph.D. thesis, Toulouse, France, Paul Sabatier University, 323 p., https://tel.archives-ouvertes.fr/tel-01080498.
Eude, A., Roddaz, M., Brichau, S., Brusset, S., Baby, P., Calderon, Y., and Soula, J.C., 2015, Timing of exhumation and deformation in the northern Peruvian eastern Andean wedge as inferred from low temperature thermochronology and balanced cross section: Tectonics, v. 34, p. 715–730.
Fleet, M.E., and Mumin, A.H., 1997, Gold-bearing arsenian pyrite and marcasite and arsenopyrite from Carlin trend gold deposits and laboratory synthesis: American Mineralogist, v. 82, p. 182–193.
Fontboté, L., 2018, Ore deposits of the central Andes: Elements, v. 14, p. 257–261.
——2020, Systematic trends in the evolution of porphyry-related Zn-Pb-(Ag) deposits: Swiss Geoscience Meeting, Zurich, 2020, Abstracts, p. 40–41.
Fontboté, L., Kouzmanov, K., Chiaradia, M., and Pokrovski, G.S., 2017, Sulfide minerals in hydrothermal deposits: Elements, v. 13, p. 97–103.
Fuchs, S., Williams-Jones, A.E., Jackson S.E., and Przybylowicz, W.J., 2016, Metal distribution in pyrobitumen of the Carbon Leader reef, Witwatersrand supergroup, South Africa; evidence for liquid hydrocarbon ore fluids: Chemical Geology, v. 426, p. 45–59.
Gaboury, D., 2013, Does gold in orogenic deposits come from pyrite in deeply buried carbon-rich sediments? Insight from volatiles in fluid inclusions: Geology, v. 41, p. 1207–1210.
George, L.L., Cook, N.J., and Ciobanu, C.L, 2017, Minor and trace elements in natural tetrahedrite-tennantite: Effects of element partitioning among base metal sulphides: Minerals, v. 7, article 17.
Goldfarb, R.J., Baker, T., Dube, B., Groves, D.I., Hart, C.J.R., and Gosselin, P., 2005, Distribution, character, and genesis of gold deposits in metamorphic terranes: Economic Geology 100th Anniversary Volume, p. 407–450.
Gregory, D.D., Large, R.R., Bath, A.B., Steadman, J.A., Wu, S., Danyushevsky, L., Bull, S.W., Holden, P., and Ireland, T.R., 2016, Trace element content of pyrite from the Kapai slate, St. Ives gold district, Western Australia: Economic Geology, v. 111, p. 1297–1320.
Gregory, D.D., Kovarik, L., Taylor, S.D., Perea, D.E., Owens, J.D., Atienza, N., and Lyons, T.W., 2022, Nanoscale trace-element zoning in pyrite framboids and implications for paleoproxy applications: Geology, v. 50, p. 736–740.
Hampel, A., 2002, The migration history of the Nazca ridge along the Peruvian active margin: A re-evaluation: Earth and Planetary Science Letters, v. 203, p. 665–679.
Hedenquist, J.W., and Lowenstern, J.B., 1994, The role of magmas in the formation of hydrothermal ore deposits: Nature, v. 370, p. 519–527.
Heinrich, C.A., 2005, The physical and chemical evolution of low-salinity magmatic fluids at the porphyry to epithermal transition: A thermodynamic study: Mineralium Deposita, v. 39, p. 864–889.
Helgeson, H.C., Kirkham, D.H., and Flowers, G.C, 1981, Theoretical prediction of the thermodynamic behavior of aqueous electrolytes at high pressures and temperatures: IV. Calculation of activity coefficients, osmotic coefficients and apparent molal and relative partial molal properties to 600°C and 5 kb: American Journal of Science, v. 281, p. 1249–1516.
Hemley, J.J., and Hunt, J.P., 1992, Hydrothermal ore-forming processes in the light of studies in rock-buffered systems: II. Some general geologic applications: Economic Geology, v. 87, p. 23–43.
Hemley, J.J., and Jones, W.R., 1964, Chemical aspects of hydrothermal alteration with emphasis on hydrogen metasomatism: Economic Geology, v. 59, p. 538–569.
Hofstra, A.H., and Cline, J.S., 2000, Characteristics and models for Carlin-type gold deposits: Reviews in Economic Geology, v. 13, p. 163–220.
Ishida, M., Romero, R., Leisen, M., Yasukawa, K., Nakamura, K., Barra, F., Reich, M., and Kato, Y., 2022, Auriferous pyrite formed by episodic fluid inputs in the Akeshi and Kasuga high-sulfidation deposits, Southern Kyushu, Japan: Mineralium Deposita, v. 57, p. 129–145.
Jacay, J., 2005, Análisis de la sedimentación del sistema cretáceo de los Andes del Perú Central: Revista del Instituto de Investigación-FIGMMG, Universidad Nacional Mayor de San Marcos, Peru, v. 8, p. 49–59.
Jaillard, E., and Jacay, J., 1989, Les Couches Chicama du Nord du Pérou: Colmatage d'un bassin né d'une collision oblique au tithonique: Comptes rendus de l'Académie des sciences. Série 2, Mécanique, Physique, Chimie, Sciences de l'univers, Sciences de la Terre, v. 308, p. 1459–1465.
John, D.A., Hofstra, A.H., Fleck, R.J., Brummer, J.E., and Saderholm, E.C., 2003, Geologic setting and genesis of the Mule Canyon low-sulfidation epithermal gold-silver deposit, north-central Nevada: Economic Geology, v. 98, p. 425–463.
Johnson, J.W., Oelkers, E.H., and Helgeson, H.C., 1992, SUPCRT92: A software package for calculating the standard molal thermodynamic properties of minerals, gases, aqueous species, and reactions from 1 to 5000 bar and 0 to 1000°C: Computers and Geoscience, v. 18, p. 899–947, updated version based on a series of subsequent papers reporting HKF parameters for most ions and aqueous complexes available online at http://geopig3.la.asu.edu:8080/GEOPIG/index.html.
Johnson, S.C., Large, R.R., Coveney, R.M., Kelley, K.D., Slack, J.F., Steadman, J.A., Gregory, D.D., Sack, P.J., and Meffre, S., 2017, Secular distribution of highly metalliferous black shales corresponds with peaks in past atmosphere oxygenation: Mineralium Deposita, v. 52, p. 791–798.
Kokh, M.A., Lopez, M., Gisquet, P., Lanzanova, A., Candaudap, F., Besson, P., and Pokrovski, G.S., 2016, Combined effect of carbon dioxide and sulfur on vapor-liquid partitioning of metals in hydrothermal systems: Geochimica et Cosmochimica Acta, v. 187, p. 311–333.
Kokh, M.A., Akinfiev, N.N., Pokrovski, G.S., Salvi, S., and Guillaume, D., 2017, The role of carbon dioxide in the transport and fractionation of metals by geological fluids: Geochimica et Cosmochimica Acta, v. 197, p. 433–466.
Kouzmanov, K., and Pokrovski, G.S., 2012, Hydrothermal controls on metal distribution in Cu(-Au-Mo) porphyry systems: Society of Economic Geologists, Special Publication 16, p. 573–618.
Kusebauch, C., Gleeson, S.A., and Oelze, M., 2019, Coupled partitioning of Au and As into pyrite controls the formation of giant Au deposits: Science Advances, v. 5, article eaav5891.
Large, R.R., Maslennikov, V.V., Robert, F., Danyushevsky, L., and Chang Z., 2007, Multistage sedimentary and metamorphic origin of pyrite and gold in the giant Sukhoi Log deposit, Lena gold province, Russia: Economic Geology, v. 102, p. 1233–1267.
Large, R.R., Danyushevsky, L., Hollit, C., Maslennikov, V., Meffre, S., Gilbert, S., Bull, S., Scott, R., Emsbo, P., Thomas, H., Singh, B., and Foster, J., 2009, Gold and trace element zonation in pyrite using a laser imaging technique: Implications for the timing of gold in orogenic and Carlin-style sediment-hosted deposits: Economic Geology, v. 104, p. 635–668.
Large, R.R., Bull, S.W., and Maslennikov, V.V., 2011, A carbonaceous sedimentary source-rock model for Carlin-type and orogenic gold deposits: Economic Geology, v. 106, p. 331–358.
Large, R.R., Thomas, H., Craw, D., Henne, A., and Henderson, S., 2012, Diagenetic pyrite as a source for metals in orogenic gold deposits, Otago schist, New Zealand: New Zealand Journal of Geology and Geophysics, v. 55, no. 2, p. 137–149.
Large, S.J.E., Bakker, E.Y.N., Weis, P., Wälle, M., Ressel, M., and Heinrich C.A., 2016, Trace elements in fluid inclusions of sediment-hosted gold deposits indicate a magmatic-hydrothermal origin of the Carlin ore trend: Geology, v. 44, p. 1015–1018.
Magoon, L.B., and Dow, W.G., 1994, The petroleum system: American Association of Petroleum Geologists (AAPG), Memoir 60, p. 3–24.
Manceau, A., Merkulova, M., Mathon, O., Glatzel, P., Murdzek, M., Batanova, V., Simionovici, A., Steinmann, S.N., and Paktunc, D., 2020, The mode of incorporation of As(-I) and Se(-I) in natural pyrite revisited: ACS Earth Space Chemistry, v. 4, p. 379–390.
Mégard, F., 1984, The Andean orogenic period and its major structures in central and northern Peru: Journal of the Geological Society of London, v. 141, p. 893–900.
Migdisov, A.A., Guo, X., Williams-Jones, A.E., Sun, C.J., Vasyukova, O., Sugiyama, I., Fuchs, S., Pearce, K., and Roback, R., 2017, Hydrocarbons as ore fluids: Geochemical Perspectives Letters, v. 5, p. 47–52.
Mikucki, E.J., 1998, Hydrothermal transport and depositional processes in Archean lode-gold systems: A review: Ore Geology Reviews, v. 13, p. 307–321.
Morishita, Y., Shimada, N., and Shimada, K., 2018, Invisible gold in arsenian pyrite from the high-grade Hishikari gold deposit, Japan: Significance of variation and distribution of Au/As ratios in pyrite: Ore Geology Reviews, v. 95, p. 79–93.
Moss, R., Scott, S.D., and Binns, R.A., 2001, Gold content of Eastern Manus basin volcanic rocks: Implications for enrichment in associated hydrothermal precipitates: Economic Geology, v. 96, p. 91–107.
Muntean, J.L., 2020, Carlin-type gold deposits in Nevada: Geologic characteristics, critical processes, and exploration: Society of Economic Geologists, Special Publication 23, p. 775–795.
Muntean, J.L., and Cline, J.S., 2018, Diversity of Carlin-style gold deposits: Reviews in Economic Geology, v. 20, p. 1–5.
Muntean, J.L., Cline, J.S., Simon, A.C., and Longo, A.A., 2011, Magmatic hydrothermal origin of Nevada's Carlin-type gold deposits: Nature

Geoscience, v. 4, p. 122–127.
Navarro Colque, P., Rivera Porras, M., and Monge Miguel, R., 2010, Geología y metalogenia del Grupo Calipuy (Volcanismo Cenozoico) Segmento Santiago de Chuco, Norte del Perú: Ministerio de Energía y Minas e INGEMMET, Boletín 28 Serie D, Estudios Regionales, 201 p.
Noble, D.C., and McKee, E.H., 1999, The Miocene metallogenic belt of central and northern Perú: Society of Economic Geologists, Special Publication 7, p. 155–193.
Noble, D.C., McKee, E.H., and Mégard, F., 1979, Early tertiary "Incaic" tectonism, uplift, and volcanic activity, Andes of Central Peru: Geological Society of America Bulletin, v. 90, p. 903–907.
Noble, D.C., McKee, E.H., Mourier, T., and Mégard, F., 1990, Cenozoic stratigraphy, magmatic activity, compressive deformation, and uplift in northern Peru: Geological Society of America Bulletin, v. 102, p. 1105–1113.
Norman, M.D., Pearson, N.J., Sharma, A., and Griffin, W.L., 1996, Quantitative analysis of trace elements in geological materials by laser ablation ICP-MS: Instrumental operating conditions and calibration values of NIST glasses: Geostandards Newsletter, v. 20, p. 247–261.
Oelkers, E.H., Benezeth, P., and Pokrovski, G.S., 2009, Thermodynamic databases for water-rock interaction: Reviews in Mineralogy and Geochemistry, v. 70, p. 1–46.
Percival, T.J., Hofstra, A.H., Gibson, P.C., Noble, D.C., Radtke, A.S., Bagby, W.C., Pickthorn, W.J., and McKee, E.H., 2018, Sedimentary rock-hosted gold deposits related to epizonal intrusions, Bau district, Island of Borneo, Sarawak, East Malaysia: Reviews in Economic Geology, v. 20, p. 259–297.
Perfetti, E., Pokrovski, G.S., Ballerat-Busserolles, K., Majer, V., and Gibert, F., 2008, Densities and heat capacities of aqueous arsenious and arsenic acid solutions to 350°C and 300 bar, and revised thermodynamic properties of $As(OH)^0_{3(aq)}$, $AsO(OH)^0_{3(aq)}$ and iron sulfarsenide minerals: Geochimica et Cosmochimica Acta, v. 72, p. 713–731.
Petroleum Experts, 2022, Petroleum engineering and structural geology software: www.petex.com/products/move-suite/.
Phillips, G.N., and Powell, R., 2013, Origin of Witwatersrand gold: A metamorphic devolatilization-hydrothermal replacement model: Applied Earth Science, v. 120, no. 3, p. 112–129.
Phillips, G.N., Groves, D.I., and Brown, I.J., 1987, Source requirements for the Golden Mile, Kalgoorlie—significance to the metamorphic replacement model for Archean gold deposits: Canadian Journal of Earth Sciences, v. 24, p. 1643–1651.
Pitcairn, I.K., Teagle, D.A.H., Craw, D., Olivo, G.R., Kerrich, R., and Brewer, T.S., 2006, Sources of metals and fluids in orogenic gold deposits: Insights from the Otago and Alpine schists, New Zealand: Economic Geology, v. 101, p. 1525–1546.
Pokrovski, G.S., and Dubessy, J., 2015, Stability and abundance of the trisulfur radical ion S_3^- in hydrothermal fluids: Earth and Planetary Sciences Letters, v. 411, p. 298–309.
Pokrovski, G.S., Kara, S., and Roux, J., 2002, Stability and solubility of arsenopyrite, FeAsS, in crustal fluids: Geochimica et Cosmochimica Acta, v. 66, p. 2361–2378.
Pokrovski, G.S., Borisova, A.Y., and Bychkov, A.Y., 2013, Speciation and transport of metals and metalloids in geological vapors: Reviews in Mineralogy and Geochemistry, v. 76, p. 165–218.
Pokrovski, G.S., Akinfiev, N.N., Borisova, A.Y., Zotov, A.V., and Kouzmanov, K., 2014, Gold speciation and transport in geological fluids: Insights from experiments and physical-chemical modelling: Geological Society of London, Special Publication 402, p. 9–70.
Pokrovski, G.S., Kokh, M.A., Guillaume, D., Borisova, A.Y., Gisquet, P., Hazemann, J.-L., Lahera, E., Del Net, W., Proux, O., Testemale, D., et al., 2015, Sulfur radical species form gold deposits on Earth: Proceedings of the National Academy of Sciences of the United States of America, v. 112, p. 13,484–13,489.
Pokrovski, G.S., Kokh, M.A., Proux, O., Hazemann, J.L., Bazarkinac, E.F., Testemale, D., Escoda, C., Boiron, M.C., Blanchard, M., Aigouy, T., Gouy, S., de Parseval, P., and Thibaut, M., 2019, The nature and partitioning of invisible gold in the pyrite-fluid system: Ore Geology Reviews, v. 109, p. 545–563.
Pokrovski, G.S., Escoda, C., Blanchard, M., Testemale, D., Hazemann, J.L., Gouy, S., Kokh, M.A., Boiron, M.C., de Parseval, F., Aigouy, T., et al., 2021, An arsenic-driven pump for invisible gold in hydrothermal systems: Geochemical Perspectives Letters, v. 17, p. 39–44.
Pokrovski, G.S., Desmaele, E., Laskar, C., Bazarkina, E.F., Testemale, D., Hazemann, J.-L., Vuilleumier, R., Seitsonen, A.P., Ferlat, G., and Saitta, A.M., 2022a, Gold speciation in hydrothermal fluids revealed by in situ high energy resolution X-ray absorption spectroscopy: American Mineralogist, v. 107, p. 369–376.
Pokrovski, G.S., Sanchez-Valle, C., Guillot, S., Borisova, A.Y., Muñoz, M., Auzende, A-L., Proux, O., Roux, J., Hazemann, J-L., Testemale, D., and Shvarov, Y.V., 2022b, Redox dynamics of subduction revealed by arsenic in serpentinite: Geochemical Perspectives Letters, v. 22, p. 36–41.
Prudhomme, A., Baby, P., Robert, A., Brichau, S., Cuipa, E., Eude, A., Calderon, Y., and Sullivan, P., 2019, Western thrusting and uplift in the northern Central Andes (Western Peruvian margin), *in* Horton, B.K., and Folguera, A., eds., Andean tectonics: Amsterdam, Elsevier, p. 299–331.
Radtke, A.S., and Scheiner, B.J., 1970, Studies of hydrothermal gold deposition (I); Carlin gold deposit, Nevada: The role of carbonaceous materials in gold deposition: Economic Geology, v. 65, p. 87–102.
Radtke, A.S., Taylor, C.M., and Christ, C.L., 1972, Chemical distribution of gold and mercury at the Carlin deposit, Nevada [abs.]: Geological Society of America Abstracts with Programs, v. 4, p. 632.
Reich, M., and Becker, U., 2006, First-principles calculations of the thermodynamic mixing properties of arsenic incorporation into pyrite and marcasite: Chemical Geology, v. 225, no. 3–4, p. 278–290.
Reich, M., Kesler, S.E., Utsunomiya, S., Palenik, C.S., Chryssoulis, S.L., and Ewing, R.C., 2005, Solubility of gold in arsenian pyrite: Geochimica et Cosmochimica Acta, v. 69, p. 2781–2796.
Rhys, D., Valli, F., Burgess, R., Heitt, D., Griesel, G., and Hart, K., 2015, Controls of fault and fold geometry on the distribution of gold mineralization on the Carlin trend, *in* Pennell, W.M., and Garside, L.J., eds., New concepts and discoveries: 2015 Symposium proceedings: Reno, Nevada, Geological Society of Nevada, p. 333–389.
Richards, J.P., 2003, Tectono-magmatic precursors for porphyry Cu-(Mo-Au) deposit formation: Economic Geology, v. 98, p. 1515–1533.
Robb, L.J., and Meyer, F.M., 1995, The Witwatersrand basin, South Africa: Geological framework and mineralization processes: Ore Geology Reviews, v. 10, p. 67–94.
Robie, R.A., and Hemingway, B.S., 1995, Thermodynamic properties of minerals and related substances at 298.15 K and 1 bar (10^5 Pascals) pressure and at higher temperatures: U.S. Geological Survey, Bulletin 2131, 461 p.
Rosenbaum, G., Giles, D., Saxon, M., Betts, P.G., Weinberg, R.F., and Duboz, C., 2005, Subduction of the Nazca Ridge and the Inca Plateau: Insights into the formation of ore deposits in Peru: Earth and Planetary Science Letters, v. 239, p. 18–32.
Rottier, B., Kouzmanov, K., Wälle, M., Bendezú, R., and Fontboté, L., 2016, Sulfide replacement processes revealed by textural and LA-ICP-MS trace element analyses: Example from the early mineralization stages at Cerro de Pasco, Peru: Economic Geology, v. 111, p. 1347–1367.
Rottier, B., Kouzmanov, K., Casanova, V., Wälle, M., and Fontboté, L., 2018, Cyclic dilution of magmatic metal-rich hypersaline fluids by magmatic low-salinity fluid: A major process generating the giant epithermal polymetallic deposit of Cerro de Pasco, Peru: Economic Geology, v. 113, p. 825–856.
Scherrenberg, A.F., Konh, B.P., Holcombe, R.J., and Rosenbaum, G., 2016, Thermotectonic history of the Marañón fold-thrust belt, Peru: Insights into mineralisation in an evolving orogeny: Tectonophysics, v. 667, p. 16–36.
Seedorff, E., Dilles, J.H., Proffett J.M., Jr., Einaudi, M.T., Zurcher, L., and Stavast, W.J.A., 2005, Porphyry deposits: Characteristics and origin of hypogene features: Economic Geology 100th Anniversary Volume, p. 251–298.
Seward, T.M., 1973, Thio complexes of gold and the transport of gold in hydrothermal ore solutions: Geochimica et Cosmochimica Acta, v. 37, p. 379–399.
Shvarov, Y.V., 2008, HCh: New potentialities for the thermodynamic simulation of geochemical systems offered by Windows: Geochemistry International, v. 46, p. 834–839.
——2015, A suite of programs, OptimA, OptimB, OptimC, and OptimS, compatible with the Unitherm database, for deriving the thermodynamic properties of aqueous species from solubility, potentiometry and spectroscopy measurements: Applied Geochemistry, v. 55, p. 17–27, www.geol.msu.ru/deps/geochems/soft/index_e.html.
Sillitoe, R.H., 2020, Gold deposit types: An overview: Society of Economic Geologists, Special Publication 23, p. 1–28.
Sillitoe, R.H., and Hedenquist, J.W., 2003, Linkages between volcanotectonic settings, ore-fluid compositions, and epithermal precious metal deposits: Society of Economic Geologists, Special Publication 10, p. 315–343.
Simmons, S.F., White, N.C., and John, D.A., 2005, Geological characteristics of epithermal precious and base metal deposits: Economic Geology 100th

Anniversary Volume, p. 485–522.
Simmons, S.F., Tutolo, B., Barker, S.L., Goldfarb, R., and Robert, F., 2020, Hydrothermal gold deposition in epithermal, Carlin, and orogenic deposits geothermal resources: Society of Economic Geologists, Special Publication 23, p. 823–845.
Simon, G., Kesler, S.E., and Chryssoulis, S., 1999, Geochemistry and textures of gold-bearing arsenian pyrite, Twin Creeks, Nevada; implications for deposition of gold in Carlin-type deposits: Economic Geology, v. 94, p. 405–421.
Stefánsson, A., and Seward, T.M., 2004, Gold(I) complexing in aqueous sulphide solutions to 500°C at 500 bar: Geochimica et Cosmochimica Acta, v. 68, p. 4121–4143.
Sverjensky, D.A., Harrison, B., and Azzolini, D., 2014, Water in the deep Earth: The dielectric constant and the solubilities of quartz and corundum to 60 kb and 1200°C: Geochimica et Cosmochimica Acta, v. 129, p. 125–145.
Sykora, S., Cooke, D.R., Meffre, S., Stephanov, A.S., Gardner, K., Scott, R., Selley, D., and Harris, A.C., 2018, Evolution of pyrite trace element compositions from porphyry-style and epithermal conditions at the Lihir gold deposit: Implications for ore genesis and mineral processing: Economic Geology, v. 113, p. 193–208.
Sylvester, P., Cabri, L.J., Tubrett, M., McMahon, G., Laflamme, J., and Peregoedova, A., 2005, Synthesis and evaluation of a fused pyrrhotite standard reference material for platinum group elements and gold analysis by laser ablation-ICP-MS: 10th International Platinum Symposium, Oulu, Finland, August 8–11, 2005, Proceedings, p. 16–20.
Tagirov, B.R., Salvi, S., Schott, J., and Baranova, N.N., 2005, Experimental study of gold-hydrosulphide complexing in aqueous solutions at 350–500°C, 500 and 1000 bars using mineral buffers: Geochimica et Cosmochimica Acta, v. 69, p. 2119–2132.
Testemale, D., Brugger, J., Liu, W., Etschmann, B., and Hazemann, J.-L., 2009, In-situ X-ray absorption study of iron (II) speciation in brines up to supercritical conditions: Chemical Geology, v. 264, p. 295–310.
Tomkins, A.G., 2013, On the source of orogenic gold: Geology, v. 41, p. 1255–1256.
Vallance, J., Balboa, M., Berna, B., Cabrera, O., Baya, C., Baby, P., and Pokrovski, G.S., 2018, Oro y material orgánico en el depósito de Shahuindo (Cajamarca, Peru): XIX Congreso Peruano de Geología, Lima, Peru, 2018, Conference Abstract, 4 p.
Velásquez, G., Béziat, D., Salvi, S., Siebenaller, L., Borisova, A.Y., Pokrovski, G.S., and de Parseval, P., 2014, Formation and deformation of pyrite and implications for gold mineralization in the El Callao district, Venezuela: Economic Geology, v. 109, p. 457–486.
Velásquez, G., Estay, H., Vela, I., Salvi, S., and Pablo, M., 2020, Metal-selective processing from the Los Sulfatos porphyry-type deposit in Chile: Co, Au, and Re recovery workflows based on advanced geochemical characterization: Minerals, v. 10, article 531.
Vigneresse, J.L., Tikoff, B., and Améglio, L., 1999, Modification of the regional stress field by magma intrusion and formation of tabular granitic plutons: Tectonophysics, v. 302, p. 203–224.
Volkov, A.V., and Sidorov, A.A., 2017, Invisible gold: Herald of the Russian Academy of Sciences, v. 87, p. 40–48.
Voute, F., Hagemann, S.G., Evans, N.J., and Villanes, C., 2019, Sulfur isotopes, trace element, and textural analyses of pyrite, arsenopyrite and base metal sulfides associated with gold mineralization in the Pataz-Parcoy district, Peru: Implication for paragenesis, fluid source, and gold deposition mechanisms: Mineralium Deposita, v. 54, p. 1077–1100.
Wells, J.D., and Mullens, T.E., 1973, Gold-bearing arsenian pyrite determined by microprobe analysis, Cortez and Carlin gold mines, Nevada: Economic Geology, v. 68, p. 187–201.
White, N.C., and Hedenquist, J.W., 1990, Epithermal environments and styles of mineralization: Variations and their causes, and guidelines for exploration: Journal of Geochemical Exploration, v. 36, p. 445–474.
Wilson, S.A., Ridley, W.I., and Koenig, A.E., 2002, Development of sulfide calibration standards for the laser ablation inductively-coupled plasma mass spectrometry technique: Journal of Analytical Atomic Spectrometry, v. 17, p. 406–409.
Wu, X., and Delbove, F., 1989, Hydrothermal synthesis of gold-bearing arsenopyrite: Economic Geology, v. 84, p. 2029–2032.
Xie, Z.J., Xia, Y., Cline, J.S., Koenig, A., Wei, D.T., Tan, Q.P., Wang, Z.P., and Muntean, J.L., 2018, Are there Carlin-type gold deposits in China? A comparison of the Guizhou, China, deposits with Nevada, USA, deposits: Reviews in Economic Geology, v. 20, p. 187–233.
Xing, Y., Brugger, J., Tomkins, A., and Shvarov, Y., 2019, Arsenic evolution as a tool for understanding formation of pyritic gold ores: Geology, v. 47, p. 335–338.
Zhou, T., Phillips, G.N., Denn, S., and Burke, S., 2010, Woodcutters goldfield: Gold in an Archaean granite, Kalgoorlie, Western Australia: Australian Journal of Earth Sciences, v. 50, p. 553–569.
Zimmer, K., Zhang, Y.L., Lu, P., Chen, Y.Y., Zhang, G.R., Dalkilic, M., and Zhu, C., 2016, SUPCRTBL: A revised and extended thermodynamic dataset and software package of SUPCRT92: Computers and Geosciences, v. 90, p. 97–111.
Zotov, A.V., Kuzmin, N.N., Reukov, V.L., and Tagirov, B.R., 2018, Stability of $AuCl_2^-$ from 25 to 1000°C at pressure to 5000 bar and consequences for hydrothermal gold mobilization: Minerals, v. 8, article 286, p. 1–15.

Jean Vallance received his Ph.D. degree from the University of Nancy, France, in 2001. In 2002 he joined the Geneva University (Switzerland) as a postdoc. From 2007 to 2013, he worked in the mineral industry as an exploration geologist in the Morococha and San Rafael deposits, Peru. In 2014, he was appointed associate professor at the Pontifical Catholic University of Peru. He currently is a part-time profesor in economic geology at the Pontifical Catholic University of Peru and teaches earth and life sciences in secondary schools in France. His research focuses on orogenic, skarn, and epithermal gold deposits.